INL/JOU-25-87006-Revision-0

Numerical Simulation of A Natural-Convection Driven Air-Cooled Reactor Cavity Cooling System Experiment

March 2026

Changing the World's Energy Future

Sinan Okyay, David Alan Reger, Victor Coppo Leite, Elia Merzari, Gerhard Strydom, Paolo Balestra

INL is a U.S. Department of Energy National Laboratory operated by Battelle Energy Alliance, LLC

INL/JOU-25-87006-Revision-0

Numerical Simulation of A Natural-Convection Driven Air-Cooled Reactor Cavity Cooling System Experiment

Sinan Okyay, David Alan Reger, Victor Coppo Leite, Elia Merzari, Gerhard Strydom, Paolo Balestra

March 2026

Idaho National Laboratory
Idaho Falls, Idaho 83415

http://www.inl.gov

Prepared for the
U.S. Department of Energy
Under DOE Idaho Operations Office
Contract DE-AC07-05ID14517

Numerical Simulation of a Natural Convection Driven Air-Cooled Reactor Cavity Cooling System Experiment

Sinan Okyay,[*,a] David Reger,[a] Victor Coppo Leite,[a] Elia Merzari,[b] Paolo Balestra,[a] and Gerhard Strydom[a]

[a] *Idaho National Laboratory, Idaho Falls, ID 83415, United States of America*

[b] *The Pennsylvania State University, University Park, PA 16803, USA*

[*]Email: sinan.okyay@inl.gov

Number of pages:	51
Number of tables:	6
Number of figures:	25

Abstract

Ensuring efficient removal of decay heat from the reactor vessel is essential for the safety of advanced reactor technologies. Several Generation IV concepts incorporate variations of reactor vessel cooling systems to achieve this objective. High-Temperature Gas-Cooled Reactors (HTGRs) utilize a Reactor Cavity Cooling System (RCCS), a passive ex-vessel system designed to operate without active components or external power during accident conditions. The RCCS removes decay heat primarily through radiative and convective heat transfer mechanisms. This study presents a comprehensive validation of a CFD Reynolds-Averaged Navier–Stokes (RANS) model for the University of Wisconsin–Madison (UW–Madison) air-cooled RCCS facility. Validation was conducted for both high- and low-power natural convection cases under a uniform heating profile. Near-wall resolution was found to be critical for accurately modeling natural convection in the RCCS: employing an all-y^+ wall treatment resulted in wall-temperature discrepancies exceeding 50°C compared to a wall-resolved mesh. Thermal-hydraulic behavior under natural and forced convection conditions was compared within the heated cavity and RCCS. Turbulence model sensitivity analysis indicates that low-Re k–ε, k–ω SST, and Reynolds Stress Transport models produce similar wall-temperature predictions. A buoyancy modeling sensitivity study revealed that the Boussinesq approximation significantly underpredicts thermal-hydraulic behavior in the RCCS. Based on these findings, modeling recommendations are provided. The validated dataset along and identified sensitivities refine the modeling natural convection in the RCCS. The information produced by this study support RCCS design, optimization and safety evaluations enabling calibration and verification of reduced-order thermal-hydraulic models.

Keywords — CFD, RCCS, STAR-CCM+, RANS, Air-cooled RCCS, Natural convection

I. INTRODUCTION

Effective removal of decay heat from the reactor vessel is a key safety aspect in the development of advanced reactor technologies. Several proposed Generation IV concepts, such as high temperature gas-cooled reactors (HTGRs), sodium-cooled fast reactors (SFRs), and lead-cooled fast reactors (LFRs), include different variations of reactor vessel cooling systems [1]. Depending on the design, exo-vessel cooling systems can operate passively, often requiring no human intervention or component operation, though some may require certain human actions such as valve manipulation. HTGRs employ a reactor cavity cooling system (RCCS), which is a passive exo-vessel cooling system that can mitigate accident consequences by using radiative and convective heat transfer. The RCCS includes vertical pipes or rectangular ducts called "risers" around the reactor pressure vessel (RPV). These risers carry out heat removal from the RPV through convective and radiative heat transfer [2]. The heat received by the RCCS is expelled into the atmosphere (ultimate heat sink) through natural convection of air inside the riser ducts. The effectiveness of the RCCS has been demonstrated via the high-temperature reactor pebble-bed module (HTR-PM) demonstration nuclear power plant. Loss-of-cooling tests validated these reactors' ability to be cooled down by simply relying on natural convection, without needing to depend on the emergency core cooling system during accident conditions [3].

Two RCCS designs are commonly employed by the industry: water-cooled and air-cooled (see Figure 1). Even though both systems utilize the same underlying heat-removal principle, they exhibit different challenges in decay heat removal. The air-cooled systems can be affected by ambient air conditions, as demonstrated in [4]. A common instability observed in these systems is flow reversal in one of the exhaust ducts, ultimately lowering the heat removal capacity of the system. Flow reversal is likely to occur in asymmetric and low-power scenarios [5, 6]. Furthermore, the water-cooled system is subject to the two-phase instabilities of water, which can reduce heat removal.

A vast amount of numerical and experimental data pertaining to RCCS studies are available in the literature. Experimental studies on an air-cooled RCCS were conducted for General Atomics' Modular High-Temperature Gas Reactor (GA-MHTGR) [5, 6, 7], while the water-cooled RCCS experimental studies are based on Frametome's steam cycle HTGR (SC-HTGR), formerly known as AREVA [8, 9]. The present work focuses on the air-cooled RCCS facility in the University of

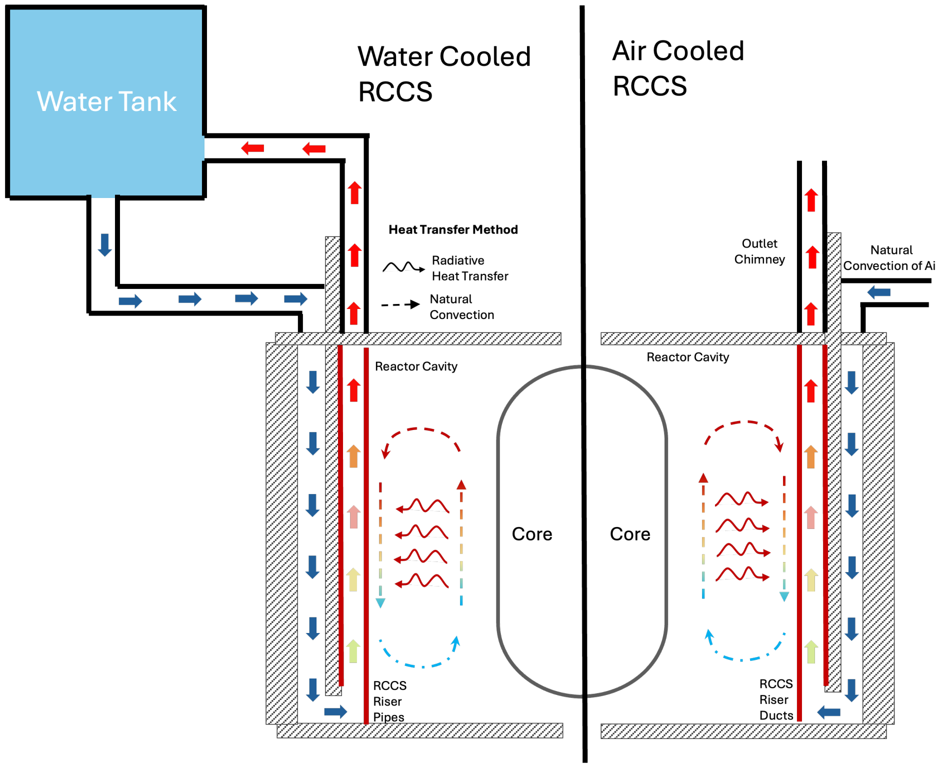

Fig. 1. The working principle behind the water- and air-cooled RCCSs.

Wisconsin-Madison (UW-Madison). The scale of the facility is shown in Figure 2.

An essential contribution to this field was made by Argonne National Laboratory (ANL) through their Natural Convection Shutdown Heat Removal Test Facility (NSTF), which has enabled experiments to be conducted at half the scale of the original design [6, 8, 10, 11, 12, 13, 14]. The NSTF experiments began with the air-cooled RCCS. The outcomes of the NSTF air-cooled RCCS experiments indicate that the overall heat removal performance remained effective despite various abnormal events such as blocked riser channels, strong asymmetries from the heated source, and moderate weather shifts. The temperature variations measured at the RPV surface, which is an indication of the maximum fuel temperature, did not increase by more than 5% of the operating values. The outcomes suggest the GA-MHTGR's air-cooled RCCS to be robust, as well as capable of maintaining safe operational temperatures under these tested conditions [6]. After the air-cooled experiments, the NSTF was converted to the water-cooled RCCS design based on Framatome's SC-HTGR [13, 14]. Initially, the water-cooled RCCS experiments were focused on single phase thermal-hydraulics. The first-year results demonstrated the verification of mass and energy balances, including the characterization of parasitic heat losses. Facility characteristics such as frictional pressure losses and transient heating response were also identified. Water-cooled RCCS experiments were conducted under both normal and depressurized loss-of-forced-cooling (DLOFC) conditions so as to demonstrate the effectiveness of the water-cooled RCCS [8]. Following this, reports pertaining to the water-cooled RCCS experiments focused on the variety of two-phase phenomena observed in the design. The experiments were conducted under various conditions, including two-phase baseline [15], parametric studies on the two-phase baseline [16], and accident conditions [17]. Each report includes a stability analysis of the experiments conducted in the corresponding year. This experimental campaign shows that Framatome's SC-HTGR RCCS can operate under various conditions and effectively perform decay heat removal.

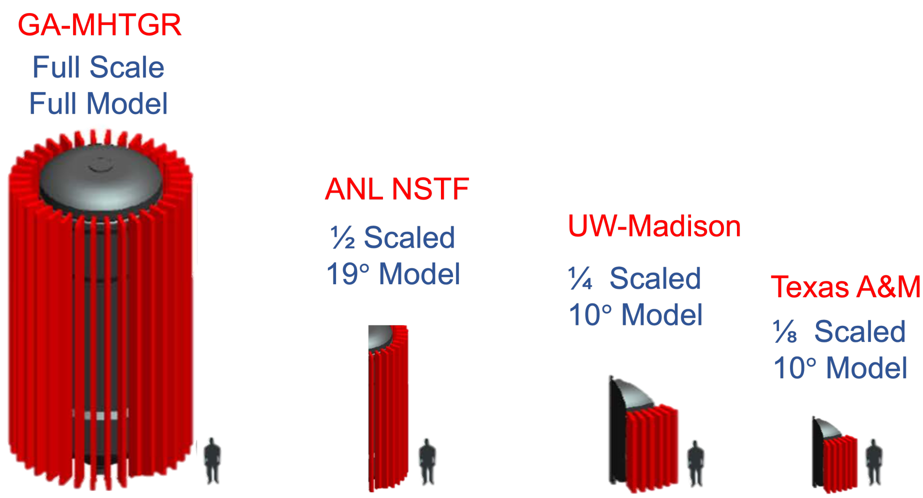

Fig. 2. Scaled representations of the GA-MHTGR RCCS.

The experimental test facility at UW-Madison represents a quarter-scale model of the GA-MHTGR design. The data from this facility are important for computational fluid dynamics (CFD) modeling. Being smaller than the NSTF makes it more computationally efficient to model with numerical tools. The experiments simulated both the air-cooled [5] and water-cooled [9, 18] RCCS designs. The air-cooled RCCS experiments included asymmetric heating cases. Instabilities similar to those observed in the NSTF were reported [5]. Water-cooled RCCS experiments were performed in this facility for single- and two-phase conditions [9]. The study confirmed that the RCCS can maintain adequate cooling for 72 hours, thus meeting the Nuclear Regulatory Commission (NRC) criteria. The authors indicated that a high level of performance can be expected at a full-scale decay heat load of 1.5 MWt, regardless of axial or asymmetric power shaping [9]. Additional experiments were conducted at Texas A&M University by employing a one-eighth-scale model (i.e., half the scale of the UW-Madison facility for the air-cooled RCCS) [19]. For these experiments, only the risers and upper plenum portion were constructed. The results indicate changes in the turbulent flow characteristics and mixing phenomena in the upper plenum, as instigated by the interactions of the parallel jets' behavior of riser ducts. In some cases, the evolution of coherent structures within the flow field was investigated by applying the Proper Orthogonal Decomposition (POD) technique [7]. Texas A&M University also constructed a water-cooled RCCS facility that was 1/23 scale of the reference water-cooled RCCS [20, 21, 22, 23]. A steady-state run was performed, confirming that natural water circulation was sufficient to remove the heat produced in the reactor vessel. They also contributed to understanding the behavior of the water in the system during both the power ramp and steady-state phases. This facility was designed as a transparent facility, thus allowing for qualitative observation of the flow mixing occurring in the RCCS system [20].

Further experiments on the RCCS can also be found in the literature. In one such experiment, conducted by the Korea Atomic Energy Research Institute (KAERI), a quarter-scale facility representing the Prismatic Modular Reactor (PMR)200's air-cooled RCCS was constructed [24]. The main outcome of this study was this RCCS design's ability to operate in the mixed convection regime, whereas previous experiments were designed to run based on either forced or natural convection [25]. Another study enabled comparison between the scaling of ANL and KAERI's air-cooled RCCSs [26]. The results indicated that the effects of mixed convection and radiative heat transfer are significant in the scaling of the test results.

Numerous studies have focused on numerical modeling of the various air- and water-cooled RCCSs (both experimental representations and conceptual designs). ANL's computational models of the NSTF air-cooled RCCS are presented in the following studies: [4, 6, 10, 27]. An ANL report [27] presents thermal-hydraulic modeling of the NSTF air-cooled RCCS by using both a system-level thermal-hydraulic code (RELAP5-3D) and a CFD code (STAR-CCM+). The results, obtained via different numerical modeling methods, were validated by the experimental results. The CFD code utilized the Reynolds-averaged Navier-Stokes (RANS) modeling strategy, and different RANS turbulence models were evaluated.

Hu et al. [4] analyzed the impact of atmospheric effects on the air-cooled NSTF RCCS, and proposed a numerical methodology for including them in the system-level thermal-hydraulic modeling. Rousseau et al. [28] compared the results obtained from two different system-level thermal-hydraulic codes (i.e., FLOWNEX and GAMMA+), with the results indicating the system-level thermal-hydraulic codes to be able to predict outcomes that are consistent with each other. The results also confirm that the system remains functional during partial blocking scenarios in the air-cooled RCCS[28]. However, a notable limitation of these codes is that they require users to accurately calculate view factors in order to estimate the radiative heat transfer from the heaters (mimics the RPV) to the risers.

Frisani et al. [29] presented a CFD analysis of an RCCS that featured circular channels instead of rectangular ones. Experimental and simulation data were produced for both the water- and air-cooled versions of the same RCCS design, showing the differences in each version's level of effectiveness [29]. Koekemoer et al. [30] investigated coupling the CFD codes with system-level thermal-hydraulic codes in order to improve simulation accuracy. Moreover, the study analyzed four different coupling strategies and compared each's overall performance against that of the others. In addition, CFD tools have been employed to increase the accuracy and fidelity of system-level thermal-hydraulic analysis codes, as documented in [31]. Freile et al. [31] considered local heat transfer effects when calculating the Nusselt number, and included a factor that accounted for the effects of non-uniform temperatures on the RPV. Their study noted that convective heat transfer is not the dominant heat transfer mode in the reactor cavity, though it significantly affects the RPV surface temperature. Therefore, accurate modeling of natural circulation is crucial to the radiative heat transfer inside the reactor cavity. Using the porous media modeling strategy, the study produced more representative heat transfer coefficients for the reactor cavity [31]. Porous media or CFD tools can be utilized to develop accurate heat transfer coefficients for the convective and radiative heat transfer inside the reactor cavity. Large eddy simulations (LES) have also been used to model partial geometries of the RCCS, including LES of rectangular ducts [32], experimental measurements of the turbulence quantities for riser ducts [33], and the outlet plenum [7] for the air-cooled RCCS.

The simulation efforts pertaining to the water-cooled systems mostly focused on the system thermal-hydraulics levels, given the complexity of modeling CFD two-phase flows. The water-cooled version of the NSTF RCCS has been modeled extensively [34, 35, 36, 37]. The computational reports from NSTF start with single-phase water-cooled RCCS modeling using system-level thermal-hydraulic tools. The numerical model was found to accurately—within 6% of the experimental measurements—predict both system and riser flow rates during single-phase, steady-state simulations [34]. This model used a CFD model of the heated cavity to more accurately represent the hydraulic losses and heat transfer values. The computational modeling reports that were written in the following years mostly focused on two-phase modeling when using system-level thermal-hydraulic tools, under various conditions such as nominal and accident scenarios [35, 36]. Ooi et al. [37] analyzed the effect of inlet throttling on system-level thermal-hydraulic modeling of the NSTF water-cooled RCCS. Their work highlights the fact that the semi-empirical correlations used in system-level codes could strongly influence model accuracy under two-phase oscillatory flows. In general, the study concluded that system-level codes can predict the two-phase flow phenomena occurring in a water-cooled RCCS.

However, there is a notable gap in the literature when it comes to CFD simulations in modeling the air-cooled RCCS at UW-Madison. Some preliminary simulations were performed in [5]; however, the CFD simulations covered in that study do not include the heat transfer that occurs in the heated cavity. To address this limitation, the present study aims to provide a multiphysics CFD model of an air-cooled RCCS experimental facility at UW–Madison. This model will incorporate both the RCCS and the heated cavity, thus offering a deeper understanding of the underlying physics involved.

The novelty of this study lies in presenting the first comprehensive CFD validation of natural convection in the UW–Madison air-cooled RCCS facility using a RANS framework. This study validates both high- and low-power natural convection cases under a uniform heat profile against experimental data. Beyond validation, it provides a systematic comparison between natural and forced convection heat removal performance in the RCCS system, offering insights into their distinct thermal-hydraulic behaviors. Furthermore, a detailed sensitivity analysis demonstrates that modeling choices—such as wall treatment, buoyancy modeling, and turbulence model selection—significantly affect prediction accuracy. These findings lead to recommended modeling practices for simulating natural convection in RCCS systems. By supplying validated RANS data and practical guidelines, this work refines the RCCS modeling and supports the improvement of lower-fidelity tools, including system-level thermal-hydraulic codes and coarse-mesh CFD approaches. Ultimately, CFD simulations such as those presented here can help enhance the accuracy of lower-fidelity codes commonly employed in design and safety analysis, enabling less conservative approaches and thereby reducing the overall cost of reactor design and development.

This work is structured as follows. Section 2 (Methods) provides an overview of the RCCS numerical model, including the governing equations, boundary conditions, and mesh. Section 3 (Results) compares the numerical model results against the experimental data, then compares the performance of various RANS models. Section 4 (Conclusion) summarizes the findings of this study and offers recommendations for future work.

II. METHODS

II.A. Governing Equations

Numerical modeling of the air-cooled RCCS at UW-Madison was performed using the RANS modeling strategy. The system thermal hydraulics can be described using the mean conservation of mass, momentum, and energy equations. The Reynolds stress term appears in the derivation of the mean conservation of momentum equation from the Navier-Stokes equation when it is derived via Reynolds decomposition. RANS models rely on the Boussinesq hypothesis (Equation 1), constituting a proportional relationship between the mean strain rate tensor and Reynolds stress. This term allows for the effects of components with fluctuating velocities (e.g., $\left\langle u_1'^2 \right\rangle$, $\left\langle u_2'^2 \right\rangle$, $\left\langle u_3'^2 \right\rangle$, $\langle u_1' u_2' \rangle$, $\langle u_1' u_3' \rangle$, and $\langle u_2' u_3' \rangle$) to be taken into account, and for average properties to be calculated without needing to resolve turbulent structures. For the derivation, refer to [38].

$$-\rho \left\langle u_i' u_j' \right\rangle = 2\mu_t S_{ij} - \frac{2}{3}\rho k \delta_{ij} \tag{1}$$

where ρ is the fluid density, μ_t is the dynamic turbulent viscosity (or eddy viscosity), k is the turbulent kinetic energy, δ_{ij} is the Kronecker delta, and S_{ij} is the mean strain rate tensor, which can be calculated per;

$$S_{ij} = \frac{1}{2}\left(\frac{\partial \langle u_i \rangle}{\partial x_j} + \frac{\partial \langle u_j \rangle}{\partial x_i}\right) \tag{2}$$

The mean conservation of mass and momentum under the Boussinesq hypothesis become the

RANS equations:

$$\nabla \cdot \langle u_j \rangle = 0 \tag{3}$$

$$\frac{\partial \langle u_i \rangle}{\partial t} + \langle u_j \rangle \cdot \nabla \langle u_i \rangle = -\frac{1}{\rho} \nabla \langle p \rangle + \nabla \cdot \left[(\nu + \nu_t) \left(\nabla \langle u_i \rangle + (\nabla \langle u_j \rangle)^\top \right) \right] + \rho \langle \mathbf{f}_i \rangle \tag{4}$$

The kinematic eddy viscosity ($\nu_t = \mu_t/\rho$), which refers to the viscosity of turbulent structures in the system, requires extra modeling for estimation. The models used in the study are introduced in the next subsection.

The conservation of energy equation becomes:

$$\frac{\partial \langle T \rangle}{\partial t} + \langle \mathbf{u} \rangle \cdot \nabla \langle T \rangle = \nabla \cdot [(\alpha + \alpha_t) \nabla \langle T \rangle] \tag{5}$$

where $\langle T \rangle$ is the Reynolds-averaged temperature, $\alpha = \frac{k}{\rho c_p}$ is the thermal diffusivity of the fluid, and α_t is the turbulent thermal diffusivity, modeled as:

$$\alpha_t = \frac{\nu_t}{\mathrm{Pr}_t} \tag{6}$$

The fluid property changes are crucial in natural convection cases. The temperature differences were around 100°C in the riser duct during the experiments, meaning the density differences significantly large in the system. The density was modeled using the low-Mach approximation based on the ideal gas law (pressure independent). The Boussinesq model was invalid for this case, since the density differences exceeded 10%. The viscosity and thermal conductivity of air were modeled using Sutherland's law. The specific heat capacity was assumed to be a constant 1005 J/kg°C for the air. The turbulent Prandtl number was assumed to be 0.85 for air.

II.A.1. Reynolds Stress Modeling

The closure problem of Reynolds stress modeling is an active area of research. Numerous models have been developed to find a good generalized approximation. The models are commonly categorized as algebraic, linear, and nonlinear eddy-viscosity models. The turbulence models covered in this section are the Spalart-Allmaras, k-ϵ, k-ω turbulence and Reynolds stress transport (RST) models. All the models solve the transport equation(s) to estimate the eddy viscosity in the Boussinesq hypothesis.

Spalart-Allmaras turbulence model

The Spalart-Allmaras model determines turbulent eddy viscosity by solving a transport equation for the modified diffusivity ($\tilde{\nu}$). This model is a one-equation model that requires an algebraic prescription of a length scale [39]. The Spalart-Allmaras model is a low-Reynolds-number model, meaning it is applied without wall functions. Thus, a fine mesh is necessary to resolve the boundary layer.

Turbulent eddy viscosity is calculated as:

$$\mu_t = \rho f_{\nu 1} \tilde{\nu} \tag{7}$$

where $f_{\nu 1}$ is the damping function [40]. The transport equation of the modified diffusivity ($\tilde{\nu}$) is calculated as

$$\frac{\partial}{\partial t}\rho\tilde{\nu} + \nabla \cdot (\rho\tilde{\nu}\langle\mathbf{u}\rangle) = \frac{1}{\sigma_{\tilde{\nu}}}\nabla \cdot [(\mu + \rho\tilde{\nu})\nabla\tilde{\nu}] + P_{\tilde{\nu}} + S_{\tilde{\nu}} \tag{8}$$

where $\tilde{\nu}$ is the modified diffusivity, $P_{\tilde{\nu}}$ is the production term, and $S_{\tilde{\nu}}$ is the source term. For the theory behind each term in the transport equation of $\tilde{\nu}$, refer to [39]. Information on the implementation can be obtained from the STARCCM+ user manual [40].

k-ϵ turbulence model

The k-ϵ turbulence model is a two-equation model that solves transport equations for the turbulent kinetic energy (k) and turbulent dissipation rate (ϵ) in order to determine the turbulent eddy viscosity. The original k-epsilon turbulence model by Jones and Launder [41] was applied with wall functions. This high-Reynolds-number approach was later modified to account for the blocking effects of the wall (viscous and buffer layer) by using both a low-Reynolds-number approach and a two-layer approach. The two-layer approach, first suggested by Rodi [42], divides the computation into two layers. In the layer next to the wall, the turbulent dissipation rate (ϵ) and the turbulent viscosity (μ_t) are specified as functions of wall distance. The values of (ϵ) specified in the near-wall layer are smoothly blended with the values computed from solving the transport equation farther from the wall. Additionally, a realizable k-ϵ is developed from the original model. This model includes a variable damping function that is applied to critical coefficients within the model. This approach allows the turbulence model to satisfy certain mathematical constraints that are consistent with the physics of turbulence, often referred to as "realizability" [43].

Turbulent eddy viscosity is calculated as:

$$\mu_t = \rho C_\mu f_\mu k T \tag{9}$$

where C_μ is the model coefficient (i.e., changes based on model, such as standard k-ϵ, realizable k-ϵ, and standard k-ϵ low Reynolds), f_μ is the damping function, and T is the turbulence time scale. The transport equation for turbulent kinetic energy and turbulent dissipation rate:

$$\frac{\partial \rho k}{\partial t} + \nabla \cdot (\rho k \langle \mathbf{u} \rangle) = \nabla \cdot \left(\mu + \frac{\mu_t}{\sigma_k} \nabla k \right) + P_k - \rho(\epsilon - \epsilon_0) + S_k \tag{10}$$

$$\frac{\partial \rho \epsilon}{\partial t} + \nabla \cdot (\rho \epsilon \langle \mathbf{u} \rangle) = \nabla \cdot \left(\mu + \frac{\mu_t}{\sigma_\epsilon} \nabla \epsilon \right) + \frac{1}{T_e} C_{\epsilon 1} P_\epsilon - C_{\epsilon 2} f_2 \rho \left(\frac{\epsilon}{T_e} - \frac{\epsilon_0}{T_0} \right) + S_\epsilon \tag{11}$$

where $\sigma_\epsilon, \sigma_k, C_{\epsilon 1}, C_{\epsilon 2}, C_t$ are model coefficients, P_k and P_ϵ are production terms, f_2 is a damping function, and S_k and S_ϵ are the source terms. More detailed information can be obtained from [40].

k-ω turbulence model

The k-ω turbulence model is another widely used two-equation model. Like the k-ϵ model, it solves for two transport equations: turbulence kinetic energy k and the specific dissipation rate ω. The original k-ω equations were proposed by D.C. Wilcox, and information on their origin and justifications can be obtained from [44, 45]. One advantage of the k-ω model is that it performs better in boundary layers under adverse pressure gradients. However, the boundary layer is more sensitive to the free stream values of ω [40]. To overcome this drawback, a k-ω model different from the standard model is proposed. This new model, named the k-ω SST model, can be derived from the k-ϵ model by applying variable substitution. The transformed equations are similar to those of the k-ϵ model, but an additional term is included to account for cross-diffusion: $\nabla k \cdot \nabla \omega$ [46]. The eddy viscosity is calculated as:

$$\mu_t = \rho k T \tag{12}$$

where T is the turbulence time scale. The transport equation for turbulent kinetic energy (k) and specific dissipation rate (ω) is calculated as:

$$\frac{\partial \rho k}{\partial t} + \nabla \cdot (\rho k \langle \mathbf{u} \rangle) = \nabla \cdot (\mu + \sigma_k \mu_t \nabla k) + P_k - \rho \beta^* f_{\beta^*} (\omega k - \omega_0 k_0) + S_k \tag{13}$$

$$\frac{\partial \rho \omega}{\partial t} + \nabla \cdot (\rho \omega \langle \mathbf{u} \rangle) = \nabla \cdot (\mu + \sigma_\omega \mu_t \nabla \omega) + P_\omega - \rho \beta f_\beta (\omega^2 - \omega_0^2) + S_\omega \tag{14}$$

where σ_ω, σ_k are model coefficients, P_k and P_ω are production terms, f_β^* is the free shear modification factor, f_β is the vortex stretching factor, S_k and S_ω are the source terms, and k_0 and ω_0 are the ambient turbulence values that counteract turbulence decay [47]. More detailed information can be obtained from [40].

Reynolds Stress Transport model

Reynolds stress transport (RST) models, also known as second-moment closure models, directly calculate the components of the Reynolds stress tensor by solving their governing transport equations. RST models approximate the stress tensor as:

$$\mathbf{T_{RANS}} = -\rho \mathbf{R} + \frac{2}{3} \mathrm{tr}(\mathbf{R}) \mathbf{I} \tag{15}$$

where ρ is the density, $\mathbf{I}$ is the identity tensor, and $\mathbf{R}$ is the Reynolds stress tensor.

$$\mathbf{R} = \begin{bmatrix} \overline{u'u'} & \overline{u'v'} & \overline{u'w'} \\ \overline{u'v'} & \overline{v'v'} & \overline{v'w'} \\ \overline{u'w'} & \overline{v'w'} & \overline{w'w'} \end{bmatrix} \tag{16}$$

RST models solve transport equations for each component of $\mathbf{R}$. These models can predict complex flows more accurately than eddy viscosity models, because they naturally account for turbulence anisotropy, streamline curvature, swirl rotation, and high strain rates.

The starting point for developing an RST model is the exact differential transport equation for the Reynolds stresses, derived by multiplying the instantaneous Navier-Stokes equations by a fluctuating property and then Reynolds-averaging their product (see [48]).

In the resulting equations, the transient, convective, and molecular diffusion terms do not require modeling [40]. The terms that must be modeled include a turbulent diffusion term, dissipation term, and pressure-strain term. The transport equation for the Reynolds stress tensor $\mathbf{R}$

is:

$$\frac{\partial}{\partial t}(\rho \mathbf{R}) + \nabla \cdot (\rho \mathbf{R} \langle \mathbf{u} \rangle) = \nabla \cdot \mathbf{D} + \mathbf{P} + \mathbf{G} - \frac{2}{3}\mathbf{I}\gamma_M + \underline{\boldsymbol{\phi}} - \rho \underline{\boldsymbol{\varepsilon}} + \mathbf{S}_R \tag{17}$$

where $\mathbf{u}$ is the mean velocity, $\mathbf{D}$ is the Reynolds stress diffusion, $\mathbf{P}$ is the turbulent production, and $\mathbf{G}$ accounts for buoyancy production. The term γ_M corresponds to the dilatation dissipation, $\boldsymbol{\phi}$ is the pressure-strain tensor, $\boldsymbol{\varepsilon}$ is the turbulent dissipation rate tensor, and $\mathbf{S}_R$ is a user-specified source term.

For the linear and quadratic pressure-strain models, dissipation is modeled as:

$$\boldsymbol{\varepsilon} = \frac{2}{3}\varepsilon \mathbf{I} \tag{18}$$

In total, seven equations are solved: six for the symmetric Reynolds stress tensor components and one for the isotropic turbulent dissipation ε.

The Elliptic Blending Reynolds Stress Transport (RST-EB) model developed by Manceau and Hanjalić [49] is a low-Reynolds number turbulence model that incorporates an inhomogeneous near-wall treatment of the quasi-linear, quadratic pressure-strain correlation. A blending function is introduced to smoothly transition between the viscous sublayer and the logarithmic region in the modeling of the pressure-strain term. This blending requires solving an elliptic partial differential equation for the blending parameter, denoted as α.

The implementation of this model in Simcenter STAR-CCM+ follows a revised formulation proposed by Lardeau and Manceau [50]. In this approach, the pressure-strain and dissipation terms are expressed as a weighted combination of near-wall and homogeneous models:

$$\underline{\boldsymbol{\phi}} - \underline{\boldsymbol{\varepsilon}} = (1-\alpha^3)(\underline{\boldsymbol{\phi}}^w - \underline{\boldsymbol{\varepsilon}}^w) + \alpha^3(\underline{\boldsymbol{\phi}}^h - \underline{\boldsymbol{\varepsilon}}^h) \tag{19}$$

Here, α is the blending parameter obtained by solving the elliptic equation:

$$\alpha - L^2 \nabla^2 \alpha = 1 \tag{20}$$

where L is the turbulence length scale. More information on the model coefficents and the treatment for near wall and the outer region please refer [40].

II.B. Numerical Modeling of UW-Madison RCCS Facility

The experimental facility built at UW–Madison is a 10° quarter-scale model of the GA-MHTGR RCCS. In scaled-down facilities, the scaling methodology is critical for ensuring similarity between the prototype and the original design. Three types of similarity should ideally be satisfied: geometric, kinematic, and dynamic. However, it is impossible to satisfy all three simultaneously, so relevant nondimensional groups are employed to preserve the dominant similarities. Because both the prototype and the original design use the same materials and fluids, similarity in material properties is maintained.

The experimental setup consists of two primary components: the RCCS and the heated cavity. The RCCS is responsible for heat removal, while the heated cavity simulates the reactor cavity in the original GA-MHTGR design. The numerical model of the experimental facility is shown in Figure 3. There are two fluid systems in the experiment: natural convection in the RCCS (shown in blue) and natural circulation within the heated cavity (shown in gray). Since there are two fluid systems, two major nondimensional groups are proposed for the scaling analysis. To maintain consistency with previous experimental studies, the same notation as in [5, 33, 6] is used.

The Richardson number is used to satisfy similarity in the RCCS. It is defined as the ratio of buoyancy forces to shear forces and can be calculated as:

$$Ri = \frac{Gr}{Re^2} = \frac{g\,\beta_{\text{riser,inlet}}\,(T_{\text{riser,outlet}} - T_{\text{riser,inlet}})\,L_h}{u_{\text{riser,inlet}}} \tag{21}$$

where g is gravitational acceleration, $\beta_{\text{riser,inlet}}$ is the thermal expansion coefficient at the riser inlet, T is the fluid temperature in the risers, L_h is the length of the heater section, and u is the fluid velocity in the risers.

The Planck number is used to satisfy similarity in the heated cavity. It represents the ratio of heat transfer by conduction to radiation and is defined as:

$$Pl = \frac{k\,\Delta T}{W\,q_h''} \tag{22}$$

where k is the thermal conductivity, ΔT is the temperature difference from the bottom to the top of the riser wall, W is the vertical distance between heaters and risers, and q_h'' is the imposed heat flux in the heaters. It is not possible to satisfy both the Richardson and Planck numbers

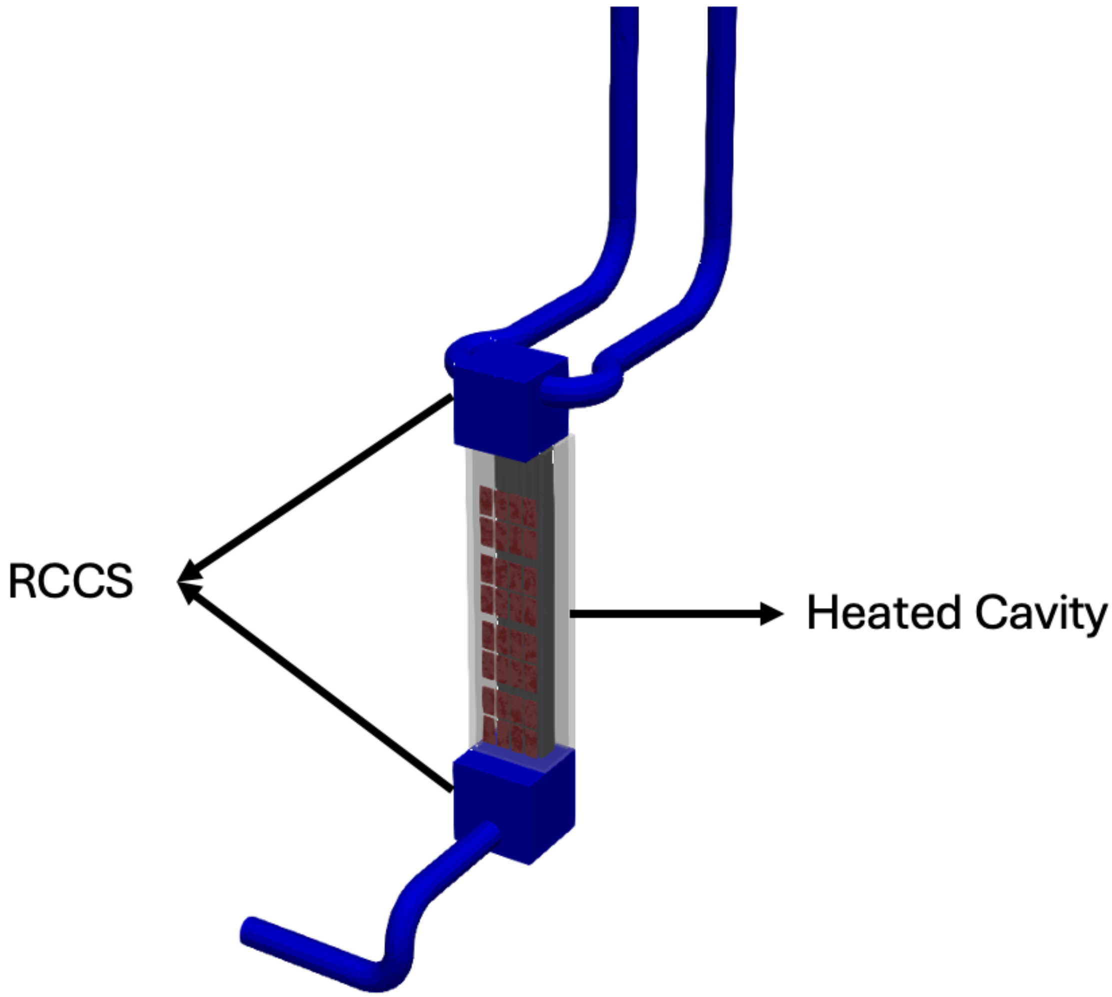

Fig. 3. Numerical model of the UW–Madison experimental facility.

simultaneously. Therefore, in this study, to remain consistent with the experiment, the Richardson number between the prototype and the scaled-down facility is preserved. The Planck number is not maintained; its ratio scales as $L_h^{-0.5}$. Details on the scaling methodology are provided in [5, 33, 6]. Additionally, a comparison of scaling laws for two different RCCS facilities is thoroughly discussed in Kim et al. [33].

There are two fluid systems in the experiments, the boundary conditions for both systems are presented separately. The boundary conditions of the RCCS are presented in Figure 5. The shaded parts represent the wall boundary condition for the temperature. The walls in the inlet pipe and plenum are adiabatic (the formulation is shown below), as the heating has not started.

$$\frac{\partial T}{\partial n} = 0 \tag{23}$$

For the riser ducts, we have an interface boundary condition between the solid walls of the riser ducts and the fluid. The conjugate heat transfer methodology is applied at the interface, where heat is transferred between the solid and fluid. The outlet plenum has Robin boundary conditions to simulate the convective cooling done by air.

$$q'' = h\left(T - T_{\infty}\right) \tag{24}$$

where h is the heat transfer coefficient and T_{∞} is the ambient temperature. The outlet plenum and the exhaust ducts are insulated. However, an unexplained heat loss exists in the system (see Table I). Therefore, the unexplained heat loss is assumed to be lost to the environment via the outlet plenum and exhaust ducts based on the discussion with experimentalists. It is assumed that the heat transfer coefficient was equal to 2 W/m^2K, and that the ambient temperature was 300 K.

This unexplained heat loss is around 15% of the total power, as seen in Table I. The first column in table represents the power supplied to the heaters while the second column shows the heat out in the table. The heat can be removed by the system, either through the RCCS or via parasitic heat losses to the environment. The heat loss can occur in the heated cavity and in the upper region of the RCCS, through the insulation material. The last column shows the difference between heat in and heat out for the experiments which shows a significant deviation. Since it is a natural convection case, the mass flow rate is function of power, and the 15% difference in power significantly affects the mass flow rate and therefore the temperature distribution.

TABLE I
Experimental data energy balance.

Name	Heat In	Heat Out		Difference
	Heaters In	Heat Removed by RCCS	Total Loss	(Heat in - Heat Out)
High Power	37.97 kW	23.10 kW	8.15 kW	6.72 kW
Low Power	19.82 kW	12.63 kW	4.66 kW	2.53 kW

The boundary conditions of the heated cavity on the axial cut of the domain are presented

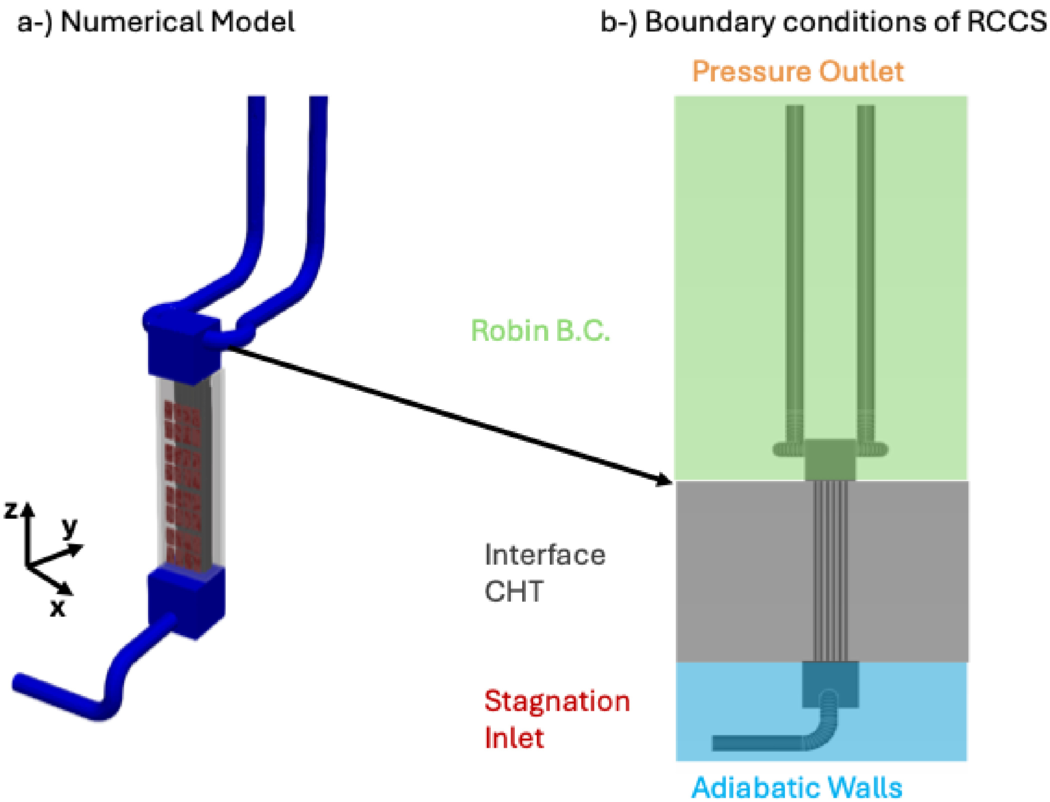

Fig. 4. Boundary conditions for RCCS.

in Figure 5. The heaters were modeled as a volumetric heat source. Natural circulation of the air inside the heated cavity was modeled, as it contributes to the heat transfer from the heaters to the riser ducts. The heat conduction equations were solved in the cavity frame, heaters, and solid walls of the riser ducts. The thermal conductivity values were taken from the experimental report [5]. Convective cooling was applied to the outer walls of the cavity frame, under the assumption that the heat transfer coefficient was equal to 15 W/m^2K and that the ambient temperature was 300 K. The heat transfer coefficient was higher for the cavity frame because in the heated cavity model the insulation material is modeled as solid, while for the outlet plenum and exhaust ducts an equivalent heat transfer coefficient is used to make the model more computationally efficient. The reason the solid is modeled in the heated cavity is to enable comparison with experimental temperatures at various locations on the solid walls.

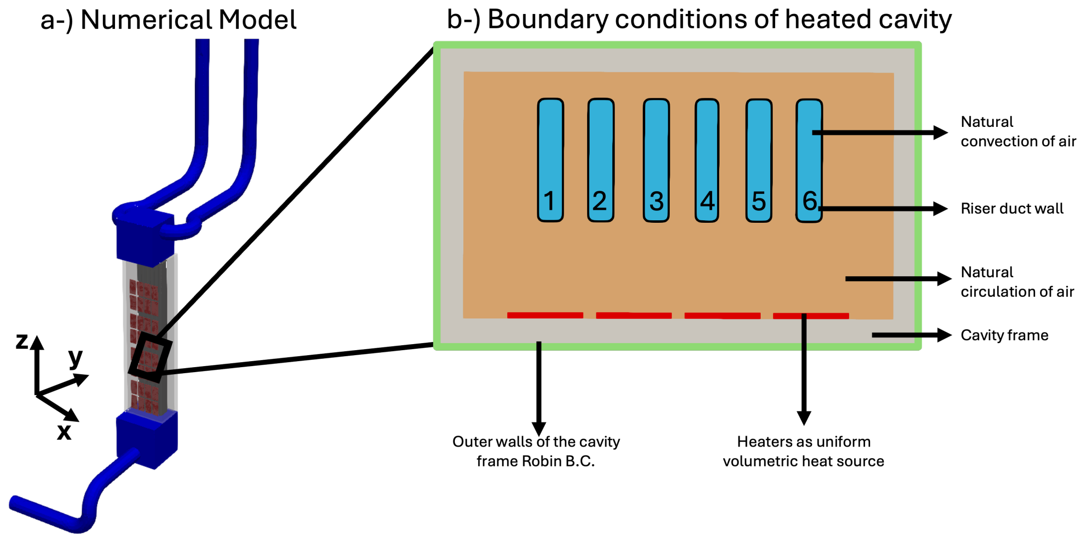

Fig. 5. Boundary conditions of the heated cavity.

II.C. Mesh

The model geometry was prepared using the CUBIT software [51]. The internal meshing tools were employed to create the mesh in STAR-CCM+. The mesh is presented in Figure 6. The polyhedral mesher is preferred. A conformal meshing strategy was employed at the interface to improve the stability for conjugate heat transfer. The mesh near the wall was created by using the prism layer meshing to resolve the fine boundary layer. The average thickness of the fluid elements was 4 mm. The mesh size of the solid was 1 mm in the riser ducts and heater, and 4 mm in the cavity frame. For the boundary layer, three prism layers were employed, for a total thickness of 1 mm. The total number of elements was around 148.31 million cells. A mesh convergence study is performed in Table II to decide the mesh base size. The bulk quantities are compared between meshes using different base sizes. The bulk temperatures of the 4_{th} riser duct ($T_{4,\text{ bulk}}$) and the outlet ($T_{\text{out, bulk}}$) are compared, along with the power removed by the RCCS and mass flow rate in each case. The mesh is considered converged at a base size of 4 mm, as the changes in power and temperature values are less than 1%

To decide the mesh resolution near the wall, a y^+study was performed. The mesh shown in Figure 6 was run with y^+ values of 0.5 and 25, using the same simulation setup. The all-y^+ treatment in the STAR-CCM+ is used for the mesh with y^+ of 25. The wall temperature showed

TABLE II
Mesh convergence study for RANS model (Standard $k-\epsilon$ Low Reynolds)

Number of elements (M)	Base Size (m)	Mass Flow Rate (kg/s)	$T_{\text{out, bulk}}$ (°C)	Power (kW)	$T_{4,\text{ bulk}}$ (°C)
65.38	0.012	0.145	185.4	23.19	238.3
78.99	0.008	0.145	185.5	23.10	241.4
148.31	0.004	0.145	185.6	23.03	242.6
241.84	0.003	0.144	185.6	23.04	242.1

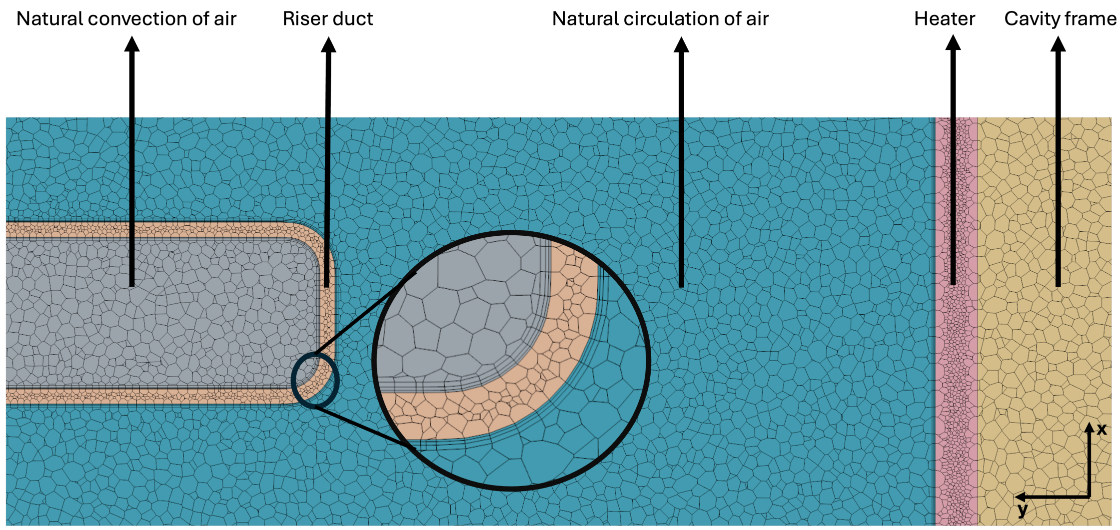

Fig. 6. STARCCM+ mesh.

differences of more than 60°C when comparing the two cases. In natural convection, the buoyancy pressure drop is balanced by the frictional pressure drop. This balance dictates the mass flow rate in the system. The majority of the frictional pressure drop stems from the viscous forces due to the wall effect. Therefore, accurate resolution near the wall is especially important in natural convection cases so as to achieve accurate mass flow rate in the system.

III. RESULTS

In this section, the numerical model from the RANS model is validated by using the available experimental data. The first part focuses on validation of the numerical model. Then heat transfer characteristics are compared between the natural convection and forced convection cases. Lastly, a comparative sensitivity analysis is performed on the turbulence models.

The simulations are run with Semi-Implicit Method for Pressure-Linked Equations (SIMPLE) algorithm for velocity-pressure coupling. The congergence criteria is 10^{-4} for velocity, energy, turbulence quantities and ray tracing for radiation, while it's 10^{-2} for pressure. These are relative

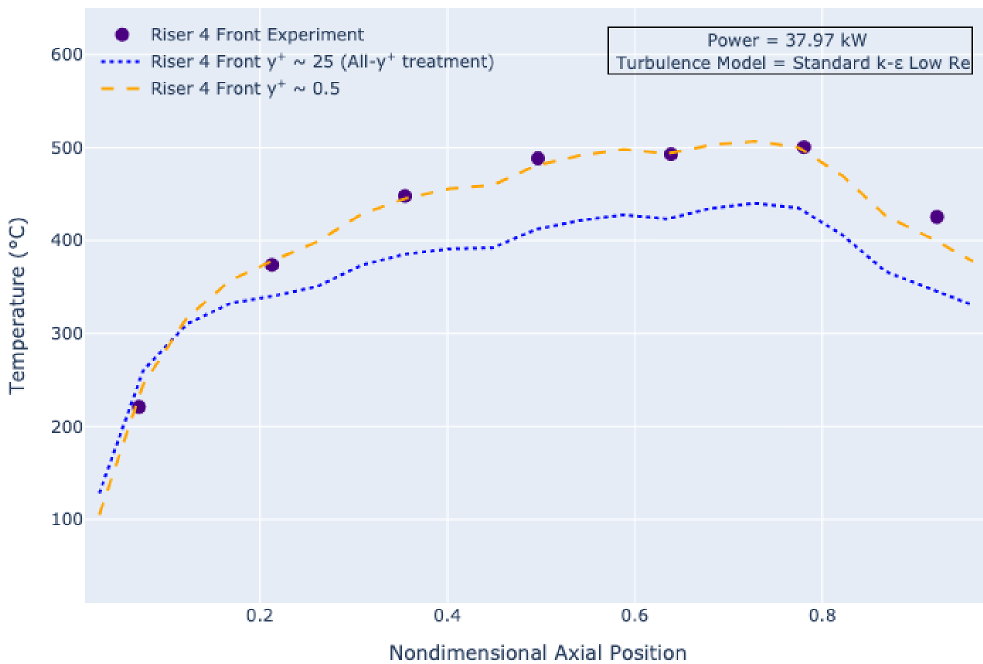

Fig. 7. y^+ study of the RCCS for the numerical model of the UW-Madison experimental facility.

to initial values, the absolute values are order to two order lower than relative value.

III.A. Validation of Natural Convection Experiments

This section compares the high-power and low-power experimental measurements against the numerical calculations. Each subsection begins by presenting the energy balance, including a mass flow rate comparison between the experiment and the simulation. Next, the wall temperature profile for the 4th riser, as measured by the experiment, is compared to the numerical calculation. Next, the front wall temperature differences between the experiment and the simulation for all risers are presented in a bar plot. The centerline temperature profile of air for the 4th riser is then examined. Subsequently, the centerline temperature differences for all risers are compared in a bar plot. Finally, the temperatures of the walls of the heated cavity are compared between the experimental data and the numerical model.

TABLE III
Setup parameters for the numerical model of UW-Madison's air-cooled RCCS.

Setup Parameters		
Modeling Strategy	RANS	
Solver	Segregated-Steady	
Methodology	Finite Volume Method	
# of Elements	148.31 Million	
Turbulence Modeling	$k-\epsilon$ Low Reynolds	
Radiation Modeling	Net Radiation Method	
Buoyancy Modeling	Low-Mach Approximation	
Wall Modeling	Wall resolved	
Experimental Test #	15	23
Power Levels	Low Power	High Power
Power	19.82 kW	37.97 kW
Inlet Temperature	301.6 K	300.2 K
Fluid Properties	Air	
	Density	Ideal Gas Law
	Viscosity	Sutherland's law
	Thermal Conductivity	Sutherland's law
	Specific Heat Capacity	Constant
	Pr_t	0.85

III.A.1. High Power

The energy balance results are shown in Table IV. The second column shows the results from the STAR-CCM+ simulation, while the third column shows the experimental measurements. The first line after the header shows the provided heat inputted to the system, which is calculated by the power controller measuring the current. The power removed by the RCCS is calculated using the temperature difference (between the inlet and outlet) and mass flow rate of the system. The results for the experiment and simulations both match.

The total heat losses in the system are calculated in the various parts of the system, primarily centering around the heated cavity. The results are consistent with the experimental results. As shown in the appendix of the experimental report, the heat loss calculations can show significant changes based on the calculation method employed [5]. Thus, an additional heat sink was implemented in the system to account for the further heat losses to the environment that occur on the outlet plenum and exhaust ducts. The additional heat sink is implemented for unaccounted heat loss in the system, making the energy balance consistent between the experiment and the simulations. Compared against the experimental results, the mass flow rate is slightly underestimated.

In Figure 8, the wall temperature distribution for riser duct 4 are compared between the

TABLE IV
High-power-case energy balance comparison.

Name	*STAR-CCM+*	*Experiment*
Heat In	37.97 kW	
Power Removed by RCCS	23.03 kW	23.10 kW
Total Heat Losses	7.94 kW	8.15 kW
Additional Heat Losses to Environment	7.00 kW	Not measured
Heat Out	37.97 kW	31.25 kW
Mass Flow Rate	0.1450 kg/s	0.1600 kg/s

simulation and the experiment. The markers represent the experimental measurements taken by thermocouples on the solid wall. The figure on the right shows the location of the thermocouples; the dashed line represents the simulation results. Since the 4th riser duct is heavily instrumented, the left, right, and back temperatures are also provided. The first subplot shows the front temperatures (i.e., the face that looks toward the heaters, which is why it is more than 100°C hotter than the other walls). Since the view factor is high between the front surface of the riser and the heater, it is expected to show significant temperature differences when compared to the other faces. The simulation temperatures closely match the experimental measurements.

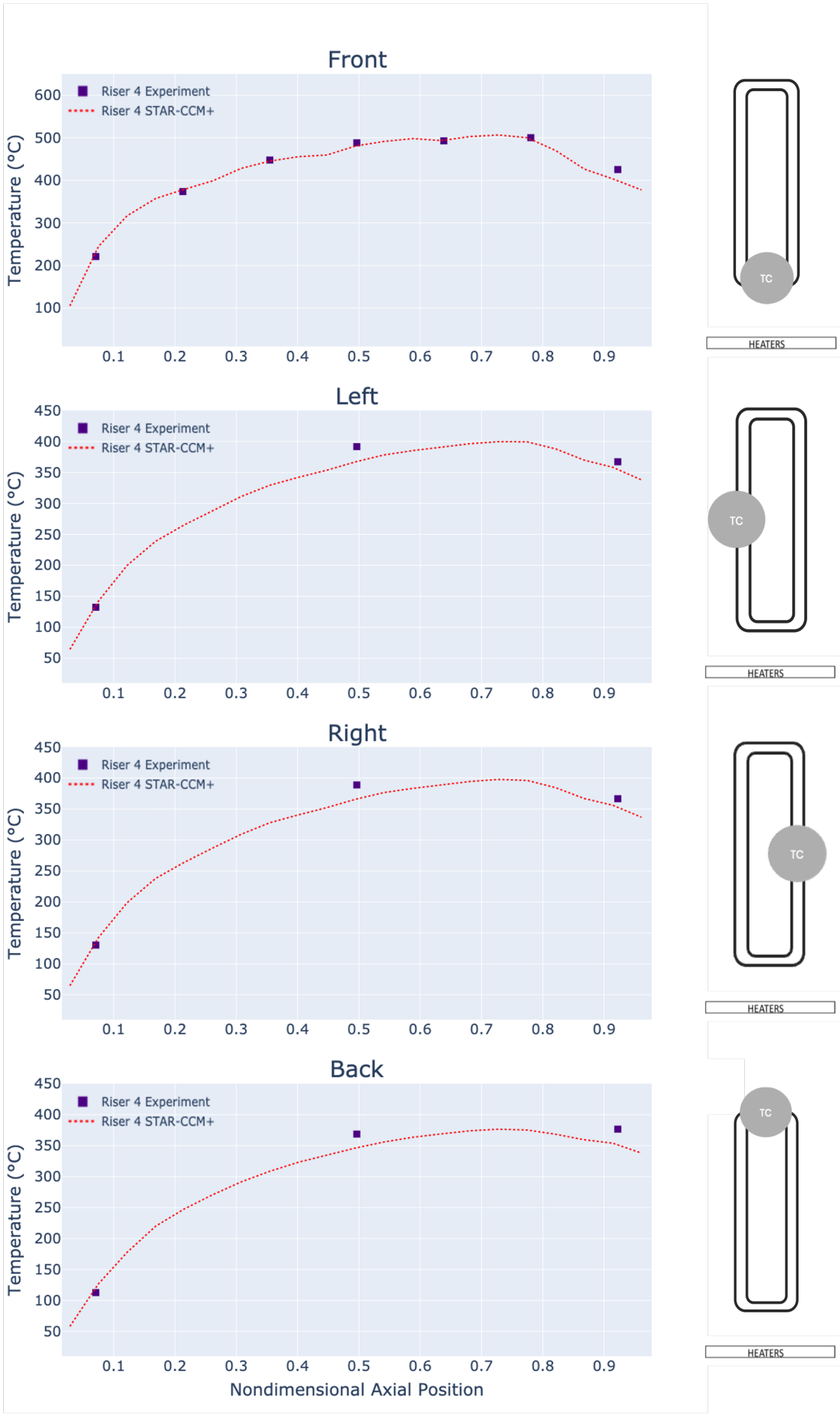

Fig. 8. High-power comparison of the 4_{th} riser wall temperatures.

A small decrease is shown in the temperature profiles at around the 0.8 non-dimensional axial position. The reason for the decrease is that the heater zone stops at that height. The consistent matching with the experiment shows that the heat transfer within the heated cavity is accurately captured. The radiative heat transfer is modeled using the net radiation methods, which have been demonstrated to be adequate for this system.

The bar plot in Figure 9 shows the front wall temperature comparisons, with each bar color representing a different riser duct, starting with the bottom marker and ending with the top one. The 4th riser has more thermocouples than do the other riser ducts. The numbers of the thermocouples are shown in the right-hand figure. The bars show the temperature difference between the experimental and simulation results. A positive difference represents overestimation; a negative one represents underestimation by the simulation temperatures. The middle heights match well with the experiments, though some deviation is shown in the bottom and top parts.

There could be multiple reasons for the difference. Overestimation in the bottom part may be caused by the sharp temperature gradient in the temperature profile, where the temperature increases from 200°C to 400°C within the first 0.2 non-dimensional axial position. The RANS models might be unable to capture this sharp temperature change. Additionally, the flow patterns in the top and bottom sections of the heated cavity may contribute to the deviation. Since the flow changes direction in those parts, the RANS models might be unable to accurately capture the changes in flow. Furthermore, experimental results could face the same uncertainty in the flow directions, making it hard to obtain representative data for those locations.

The centerline air temperatures for the 4th riser are presented in Figure 10. The results match with the experimental results. The trend is underestimation at the bottom and middle sections, and overestimation at the end of the channel.

Figure 11 compares the air centerline temperatures of all the risers. The results are similar to those observed for the 4th riser. There is a slight underestimation at the entrance of the channel, whereas the simulation overpredicts the centerline temperature at the end of the channel. One reason for this is the mismatch in mass flow rate. The mass flow rate is lower than the experimental measurements, thus causing the elevated temperatures at the end of the riser ducts. Additionally, a simple turbulent heat flux model was adopted for this analysis, and can contribute to the error in the natural convection setups.

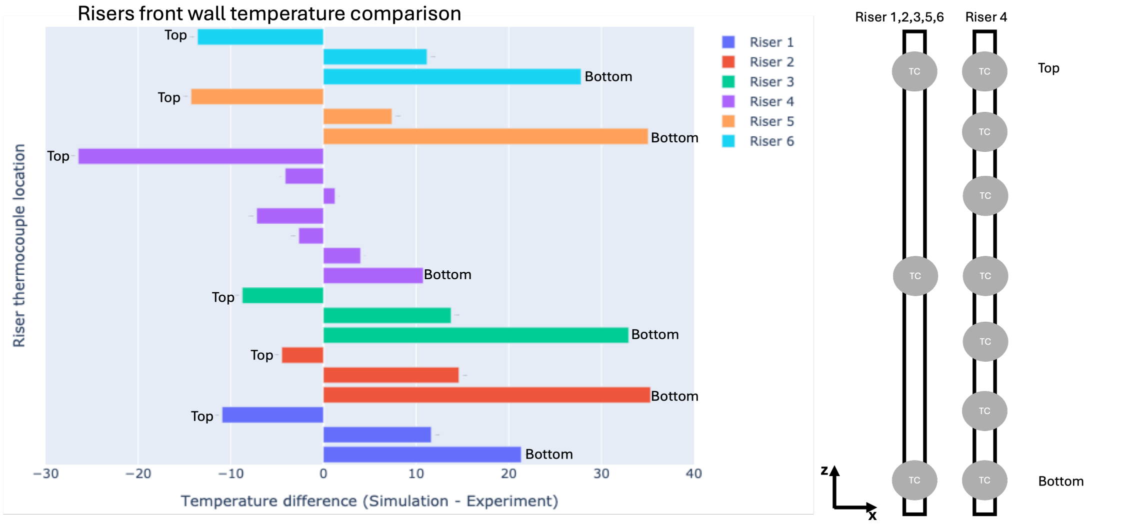

Fig. 9. High-power front wall comparison of all riser ducts.

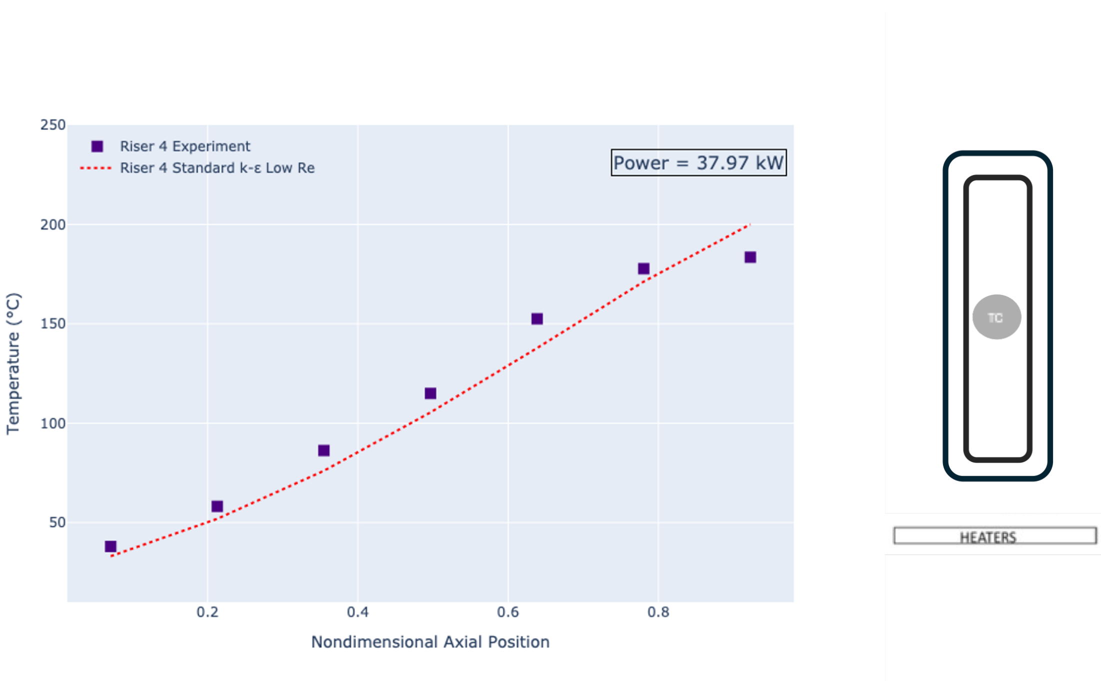

Fig. 10. High-power comparison of the 4_{th} riser centerline temperatures.

The final part of this section compares the wall temperatures in the heated cavity. The temperatures of the left, right, and back walls at the middle of the domain were all calculated. The thermocouple positions can be obtained from the experimental report [5] and presented in

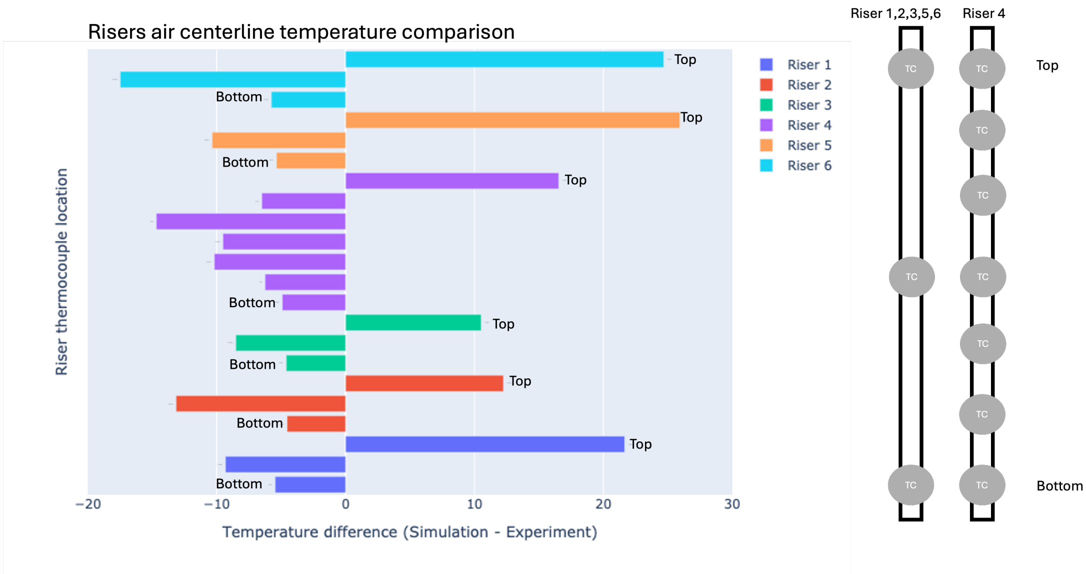

Fig. 11. High-power comparison of the air centerline temperatures of all the riser ducts.

Figure 12. Table V shows the wall temperature difference between the heated cavity and the experiment. The simulation overestimates the left and right wall temperatures but underestimates the back wall temperature. The dominant heat transfer mechanism in the heated cavity is radiative heat transfer. Since the wall temperatures match, the radiative heat transfer is expected to be accurate. The slight difference could be due to uncertainty in the insulation material thickness or in the heat transfer coefficient used for the outside of the heated cavity.

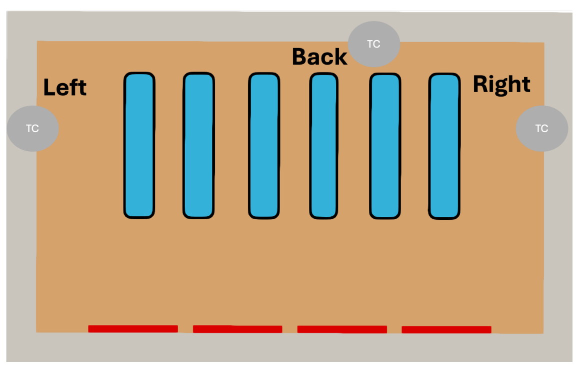

Fig. 12. Heated cavity wall thermocouple locations.

TABLE V
High-power heated cavity wall comparison.

Name	STAR-CCM+ (°C)	Experiment (°C)
Left	461	431
Right	457	429
Back	378	387

III.A.2. Low Power

The same model was run for the low-power scenario. The power in this case was 19.82 kW. The energy balance results are shown in Table VI. The power removed by the RCCS is slightly underestimated in this case, and thus so is the mass flow rate. Considering the complexity of the case, the model performs adequately. The numerical model may overestimate the heat going to the additional heat sink which covers the heat losses that goes to environment through outlet plenum and exhaust ducts.

TABLE VI
Low-power-case energy balance comparison.

Name	*STAR-CCM+*	*Experiment*
Heat In	19.82 kW	
Power Removed by RCCS	10.33 kW	12.63 kW
Total Heat Losses	4.87 kW	4.66 kW
Additional Heat Losses to Environment	4.62 kW	Not measured
Heat Out	19.82 kW	17.29 kW
Mass Flow Rate	0.1033 kg/s	0.1389 kg/s

In Figure 13, the wall temperature profiles for riser duct 4 are compared between the simulation and the experiment. The numerical model is able to capture the same trends observed in the experiments. A slight underestimation of temperature is caused by underestimation of the mass flow rate. Since less power is going to the RCCS, this slight underestimation of the temperature values is expected. In general, the simulation successfully reflects the same behavior as the experimental measurements.

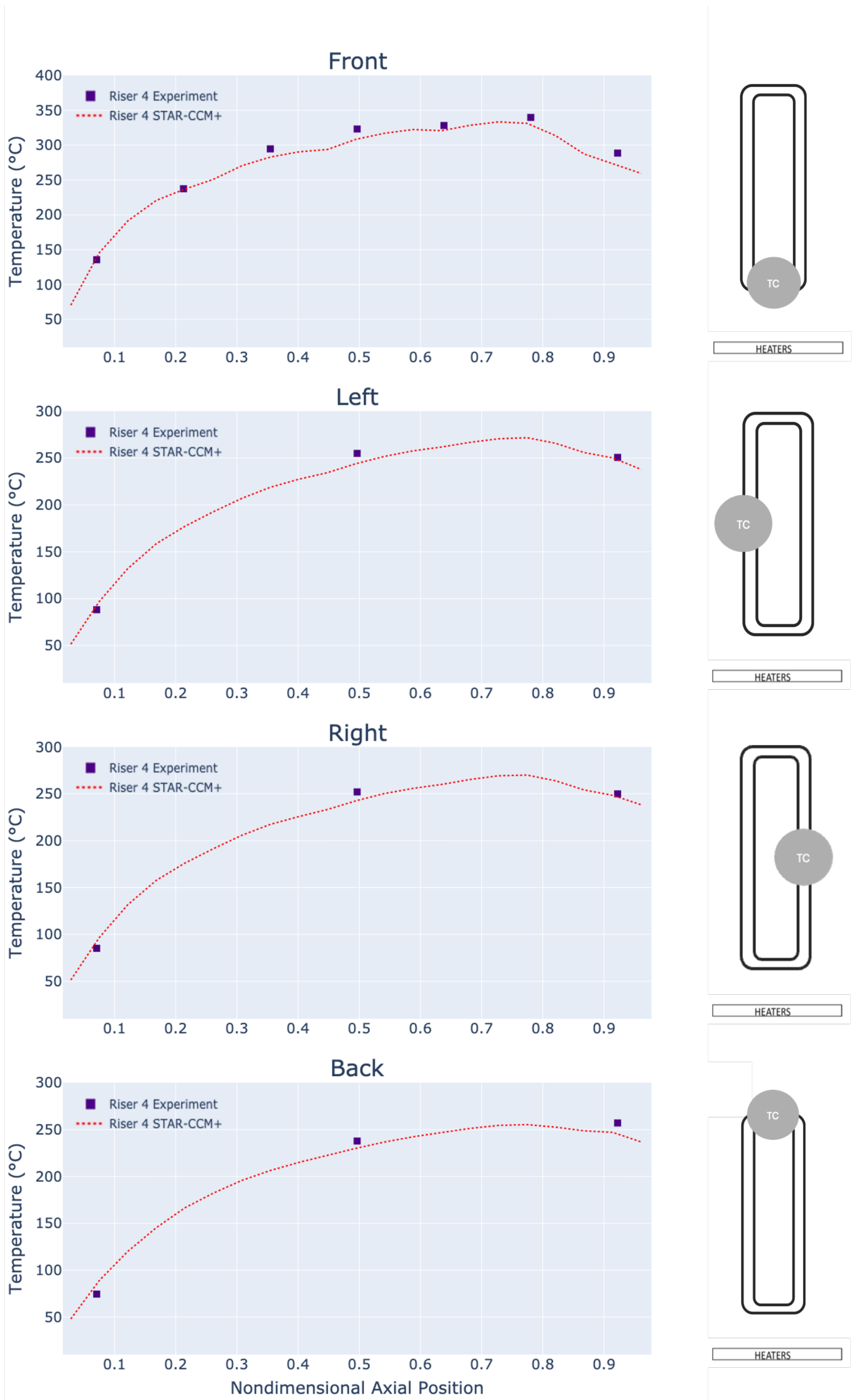

Fig. 13. Low-power comparison of the 4_{th} riser wall temperatures.

The wall temperature profiles for all the riser ducts are compared in Figure 14 via a bar graphs. Each bar shows the temperature difference between the experiment and the simulation. The temperature values are overestimated in the first point where the sharp gradient occurs. A slightly lower temperature value is then observed in comparison to the experiment.

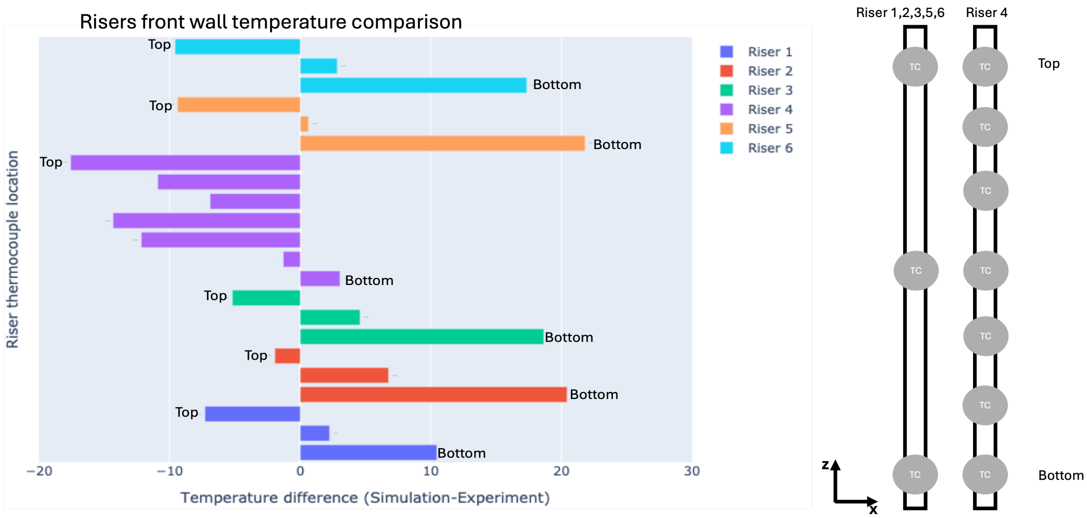

Fig. 14. Low-power front wall comparison of all the riser ducts.

The air centerline temperatures for the 4_{th} riser are compared in the figure below. The temperature values match the experimental results for the lower half of the channel, but the upper half shows some deviation. The deviation increases at the end of the channel with more heating. A main reason for this could be the lower mass flow rate. In addition, a very simple turbulent heat flux model was used in this numerical model. Therefore, the simple gradient hypothesis could be contributing to the deviation.

The air centerline temperatures for all the riser ducts are compared in Figure 16. All riser ducts show the same behavior as previously observed in the 4_{th} riser duct. In all the riser ducts, there is a trend in which the deviation from the experimental results increases with heating. The maximum deviation is reached at the end of the channel. In addition to the lower total mass flow rate, mixing in the outlet plenum of the riser ducts can also contribute to this deviation.

The heated cavity wall temperatures are compared in Table 17. The wall temperatures on the heated cavity are slightly overestimated, but generally match the experimental measurements. At both power levels, the heated cavity and riser duct wall temperature predictions are consistent

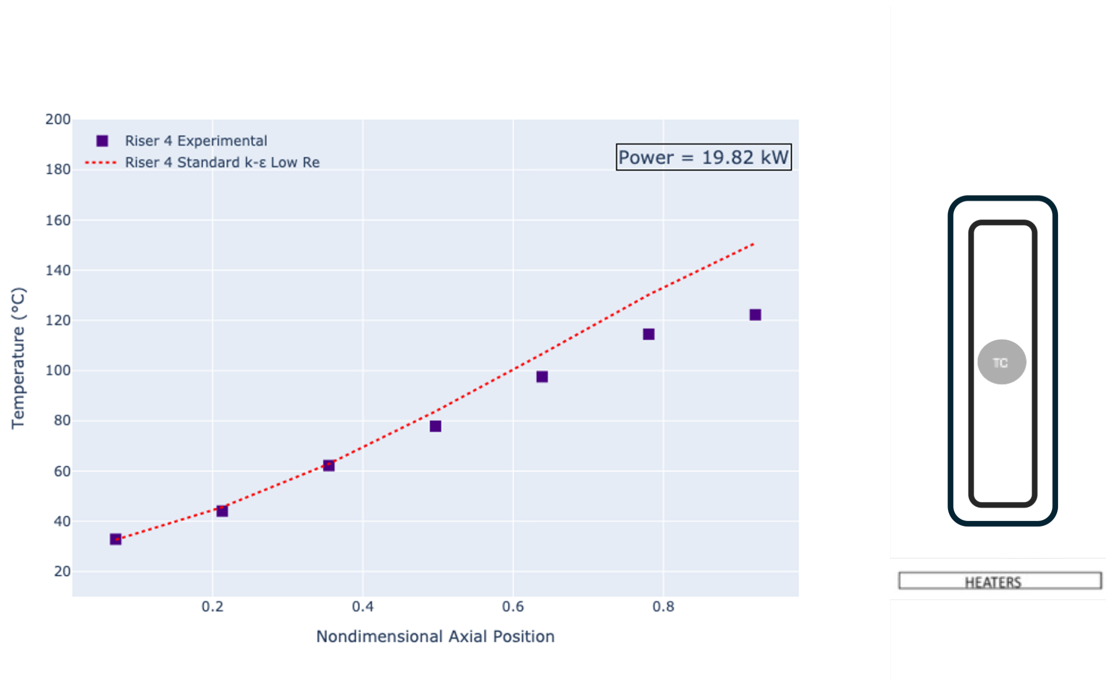

Fig. 15. Low-power comparison of the 4_{th} riser centerline temperatures.

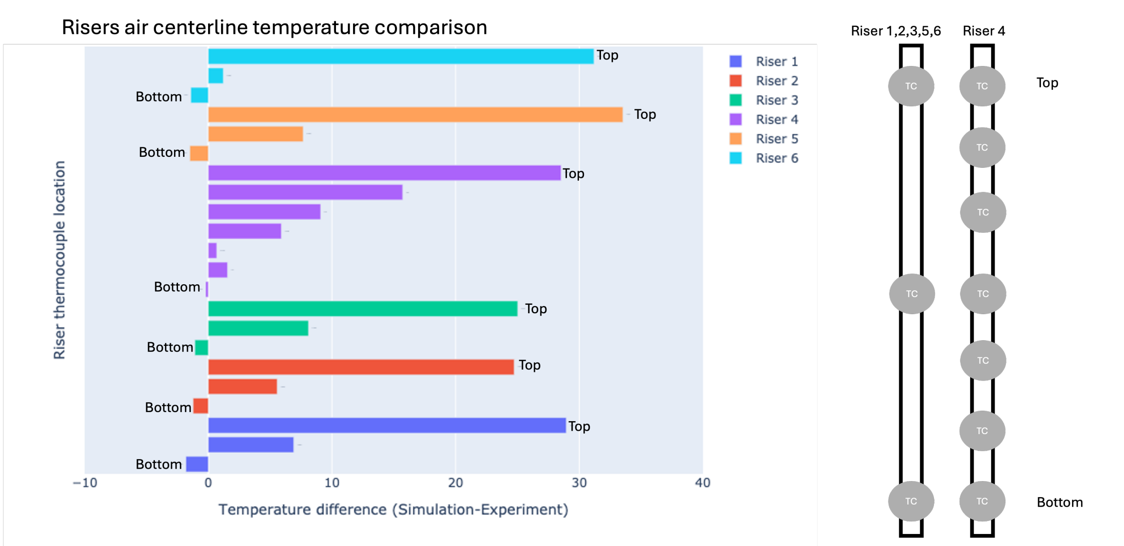

Fig. 16. Low-power comparison of the air centerline temperatures of all the riser ducts.

with the experimental measurements. Based on these results, the RANS model is able to predict the correct temperature distribution within the heated cavity.

Fig. 17. Low-power heated cavity wall comparison.

Name	STAR-CCM+ (°C)	Experiment (°C)
Left	305	290
Right	302	285
Back	251	256

III.B. Comparison of flow characteristics in natural and forced convection

The flow characteristics of natural and forced convection cases are compared within the RCCS riser ducts. The Reynolds number ($Re = \rho V_{\text{riser}} D_{h,\text{riser}}/\mu$) is calculated. The hydraulic diameter calculated as 0.0754 m for the 4th riser duct. The Reynolds number for forced convection is approximately 20,000, while it is around 7,000 for natural convection. This decrease in Reynolds number is expected, as the flow in the natural convection case is not driven by a pump.

Figure 18 shows the temperature distributions in the riser ducts for forced convection (top) and natural convection (bottom). The temperature distributions generally show similar behavior between the two cases. In both scenarios, the highest temperatures occur on the front face of the riser ducts, as this face is directly exposed to the heaters.

The internal riser ducts (2, 3, 4, and 5; see Figure 5 for numbering) exhibit similar temperature profiles: the face oriented toward the heaters is the hottest, while the other faces are progressively cooler, with the back face being the coolest due to its low view factor with respect to the heaters.

The corner riser ducts (1 and 6) show increased temperatures on their side walls, as these faces are exposed to the heated cavity. This is likely due to radiative heat transfer between the heated cavity walls and the side faces of the risers.

Such asymmetry is not expected in the actual RCCS design, as the side walls of the heated cavity do not exist in the real system. In the actual configuration, the reactor pressure vessel is fully surrounded by riser ducts, eliminating direct exposure of side walls to the heated cavity.

Figure 19 shows a comparison of the velocity fields for forced and natural convection. Significant differences are observed due to the distinct driving mechanisms in each case.

The forced convection velocity field is consistent with expectations for internal forced flows, where the velocity profile is parabolic, increasing from the wall to a maximum near the center. Some asymmetries are present, likely caused by variations in temperature-dependent properties

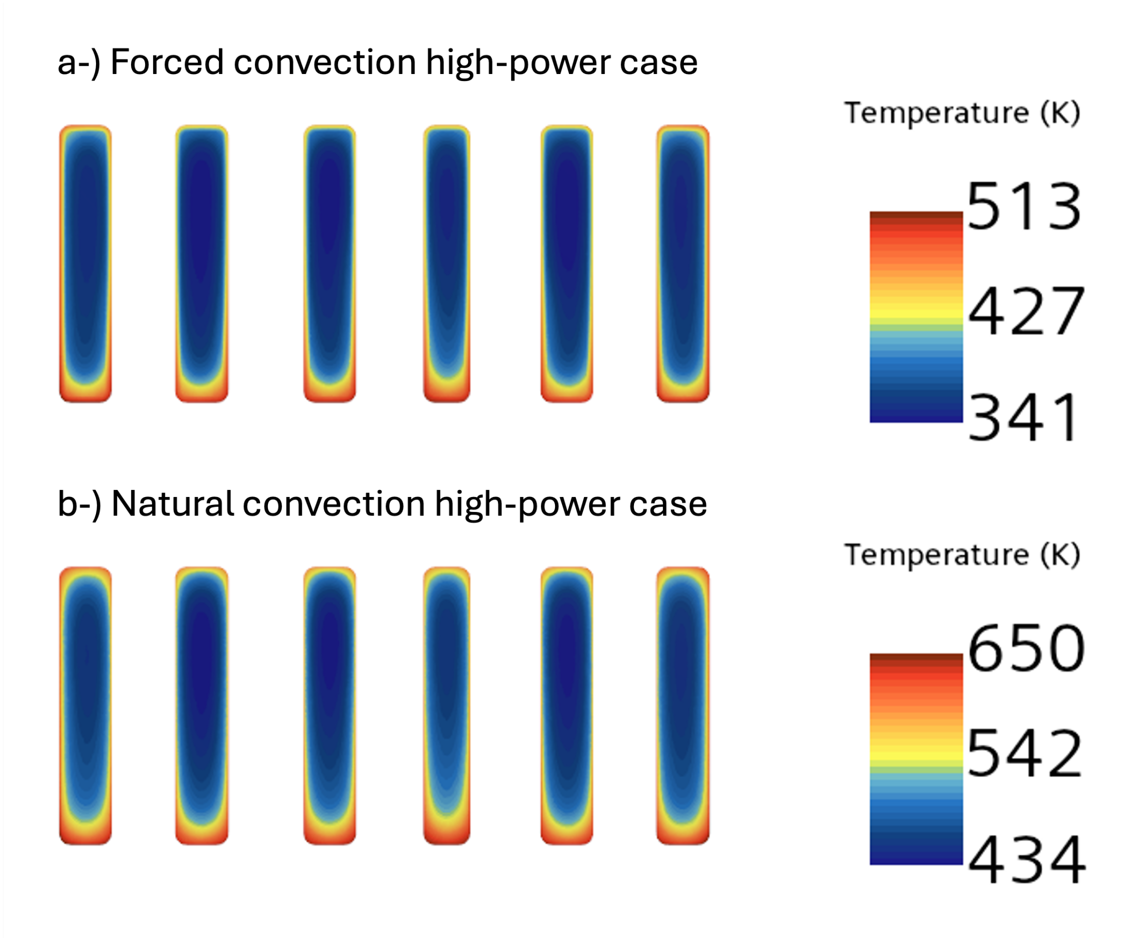

Fig. 18. Comparison of the velocity profiles of riser ducts between the forced and natural convection high-power case.

due to uneven heating and jet interactions at the outlet plenum.

In the natural convection simulations, the velocity magnitude decreases significantly, and the shape of the velocity field changes. The maximum velocity shifts toward the wall, specifically the hottest wall of the riser ducts, where buoyancy forces are stronger compared to the center of the channel.

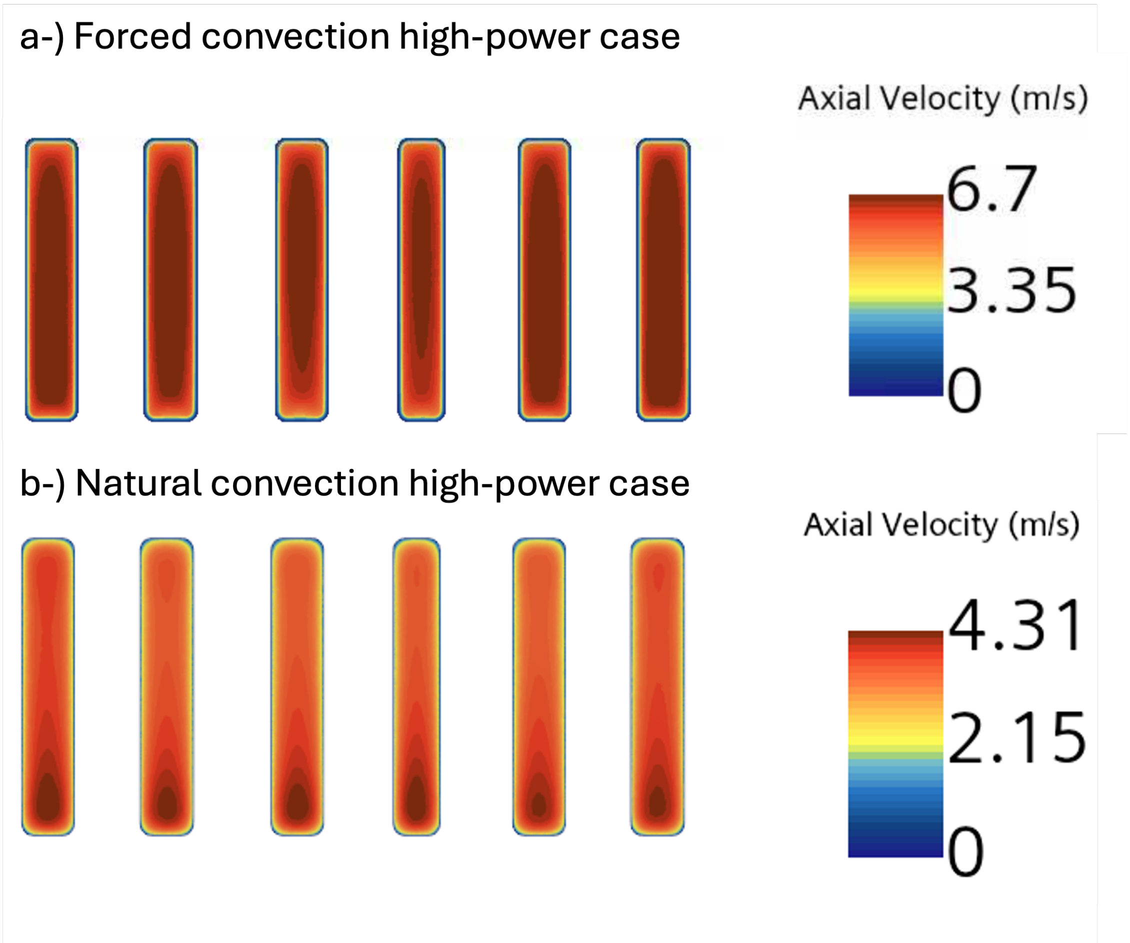

Fig. 19. Comparison of the turbulent kinetic energy profiles of riser ducts between the forced and natural convection high-power case.

The final comparison highlights the differences in turbulent kinetic energy (TKE) profiles between the forced and natural convection cases. It should be noted that the forced convection case was run using the $k-\omega$ SST model with wall functions, while the natural convection cases were simulated using the standard k–ϵ Low Reynolds number model with a boundary-resolved mesh near the wall region.

In the forced convection case, high values of turbulent kinetic energy are observed around the side walls. The TKE values are significantly higher than those in the natural convection case.

In the natural convection case, the maximum TKE value occurs closer to the region of maximum velocity. The overall TKE is much lower compared to the forced convection case, which is expected since the Reynolds number is approximately one-third that of the forced convection scenario.

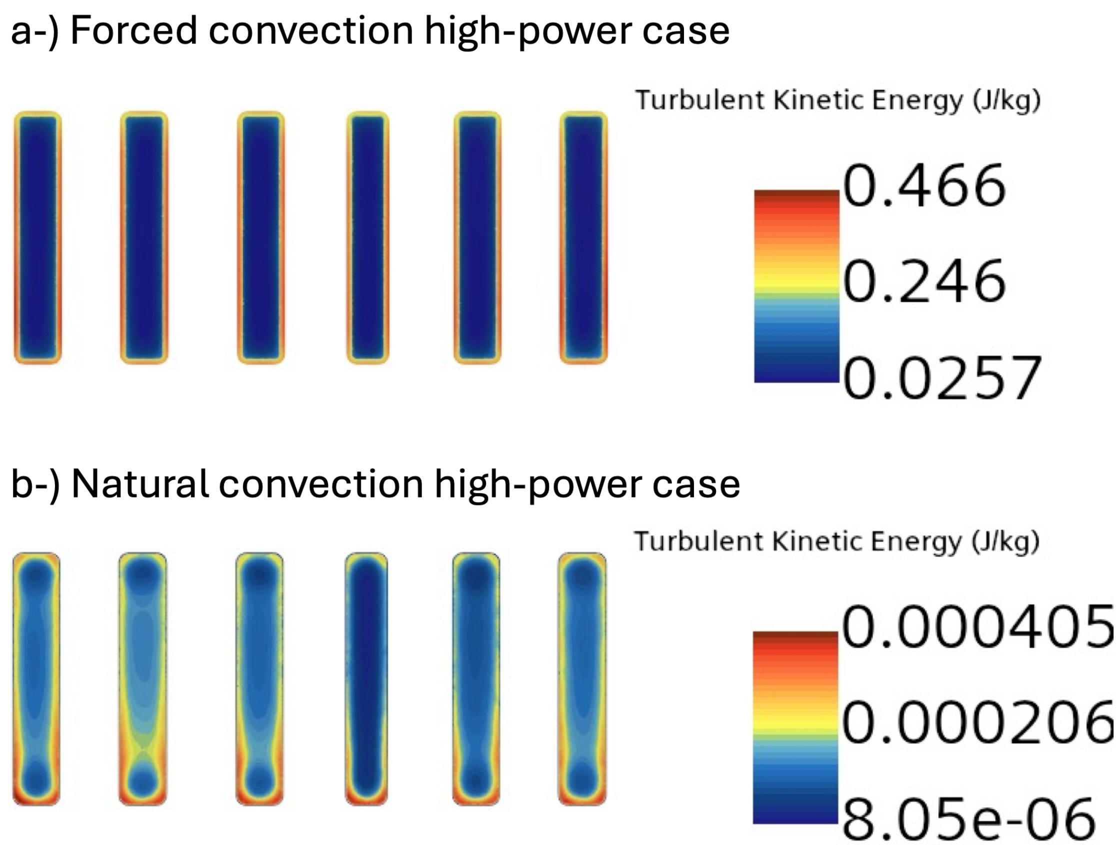

Fig. 20. Comparison of the turbulent kinetic energy profiles of riser ducts between the forced and natural convection high-power case.

III.C. Heat transfer modes in the heated cavity

This section presents the heat transfer mechanisms between the heaters and the riser ducts in the heated cavity. Figure 21 compares convective and radiative heat transfer for both low- and high-power scenarios under forced and natural convection conditions. The horizontal axis shows the fraction of total power removed by the RCCS for each case, with the power supplied to the system indicated in parentheses. The vertical axis shows the percentage of radiative (green bars) and convective (blue bars) heat transfer relative to the total power removed by the RCCS.

The forced convection results have already been presented in [52]. Figure 21 shows the dominant heat transfer mechanism to be radiative heat transfer in the heated cavity. Radiation is more pronounced in the natural convection cases than in the forced convection cases. The contribution of the radiative heat transfer is around 88% in the natural convection cases, but around 78% in the forced convection cases. Both the natural and forced convection cases exhibit the same behavior as the power increases. In both setups, the contribution of radiation increases, mainly because radiative heat transfer changes with the fourth power of the temperature.

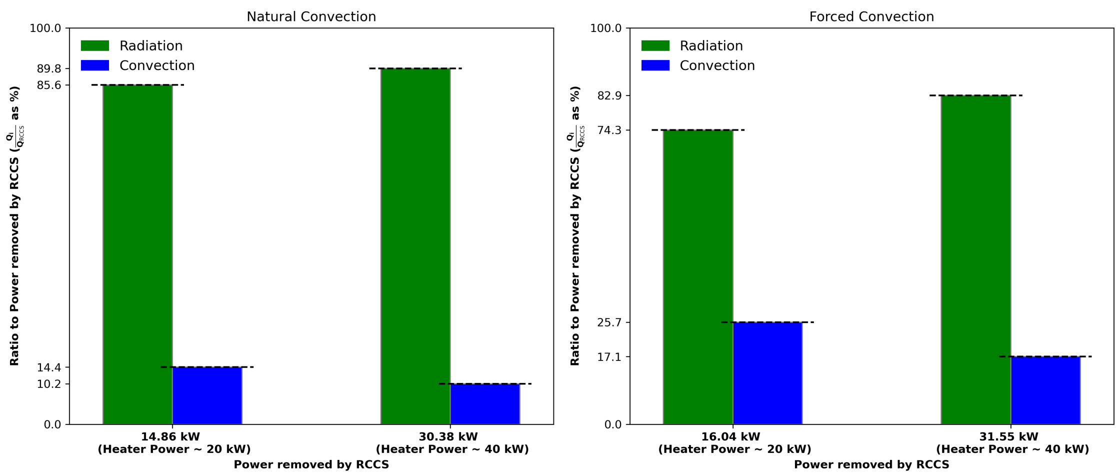

Fig. 21. Heat transfer modes between the heaters and RCCS.

III.D. RANS turbulence modeling strategy

This section presents the sensitivity of the RANS turbulence models. Multiple modeling strategies have been tested: standard k-ϵ low Reynolds, realizable k-ϵ (two layer), k-ω SST, Spalart-Allmaras and Reynold stress transport with elliptic blending. These turbulence models entail different levels of complexity and assumptions for modeling the effect of the fluctuating components on averaged fields. The calculations used were on the front wall and air centerline temperatures for the 4th riser.

Figure 22 shows the effect on the front wall temperatures. Most of the models are able to predict temperatures close to the experimental measurements. The following models produced consistent results with each other: the standard k-ϵ low Reynolds, k-ω SST, and Reynolds stress transport with elliptic blending models. A strong deviation is observed in the Spalart-Allmaras and realizable k-ϵ (two-layer) models. Since the Spalart-Allmaras model is the simplest model employed in this study, the deviation from the results is expected. The realizable k-ϵ (two-layer) model is included here since it is the default model in STAR-CCM+. This model shows the largest deviation from the experimental measurements of wall temperatures. The realizable k-ϵ (two-layer) model is an alternative to low Reynolds number RANS models and is usually run on a coarser mesh. Therefore, the deviation could be caused by using a mesh grid appropriate for low Reynolds number RANS models. The main difference between the models is seen in the sharp temperature gradient before the 0.2 non-dimensional axial position. All models predict highe temperatures in this region compared to experimental measurements.

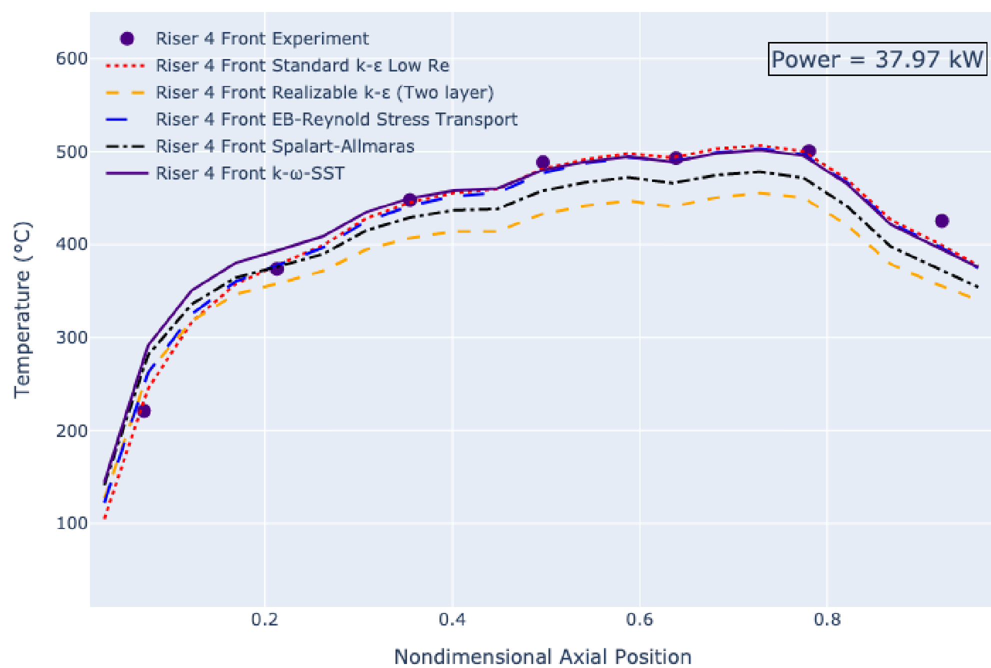

Fig. 22. Effect of RANS turbulence models on the front wall temperatures of the 4_{th} riser duct.

Figure 23 compares the air centerline temperatures for all the turbulence models. All RANS models were able to predict the same trend as observed in the experimental outcomes. Most models tended to underpredict the temperature profile up until the last measurement point. At the last measurement point, all models overpredicted the temperature. The k-ω SST model best matches the experimental temperature distribution. (It should be noted that this is not the bulk temperature but the centerline temperature. Therefore, differences in this distribution do not indicate that less energy is going into the riser duct.) Since we have highly asymmetrically heated riser duct walls, the RANS turbulence models were expected to show some differences in the temperature distribution. Additionally using the simple gradient diffusion hypthosesis may contribute to deviation from expeirmental measurements. Additionally, the use of the simple gradient diffusion hypothesis may contribute to deviations from the experimental measurements. While more advanced turbulent heat flux models could potentially improve the results, the algebraic turbulent heat flux model in STAR-CCM+ is currently not available for most RANS turbulence modeling strategies and can only be used with the Boussinesq approximation for buoyancy modeling. Since we have signicant density differences in the system Boussinesq approximation is not expected to valid for this case, Consequently, the analysis with algebraic heat flux modeling is not included in this analysis.

III.E. Bouyancy modeling

In natural convection systems, fluid is driven by buoyancy force, and correct modeling of this force has a crucial effect on the accuracy of the results. The buoyancy force is balanced by the frictional losses in the system. This balance prescribes the mass flow rate in the system, which is not known a priori before running the simulation. Since heat transfer and fluid flow are coupled in natural convection systems, accurately modeling the buoyancy forces is arguably the most important modeling preference for achieving physical results.

Therefore, two common modeling strategies are tested in the low-power convection case–Boussinesq approximation and Low-Mach approximation–to evaluate the effect of buoyancy modeling on the accuracy of the results. The Boussinesq approximation assumes that fluid density changes linearly with sufficiently small temperature differences in the system. Density variations are then neglected in the Navier–Stokes equations but accounted for in the body force gravity term.

The Low Mach approximation is a mathematical model used to simulate fluid flows where the Mach number is low (less than approximately 0.2), indicating that compressibility effects are present but not dominant. In this formulation, density is typically expressed as a function of tem-

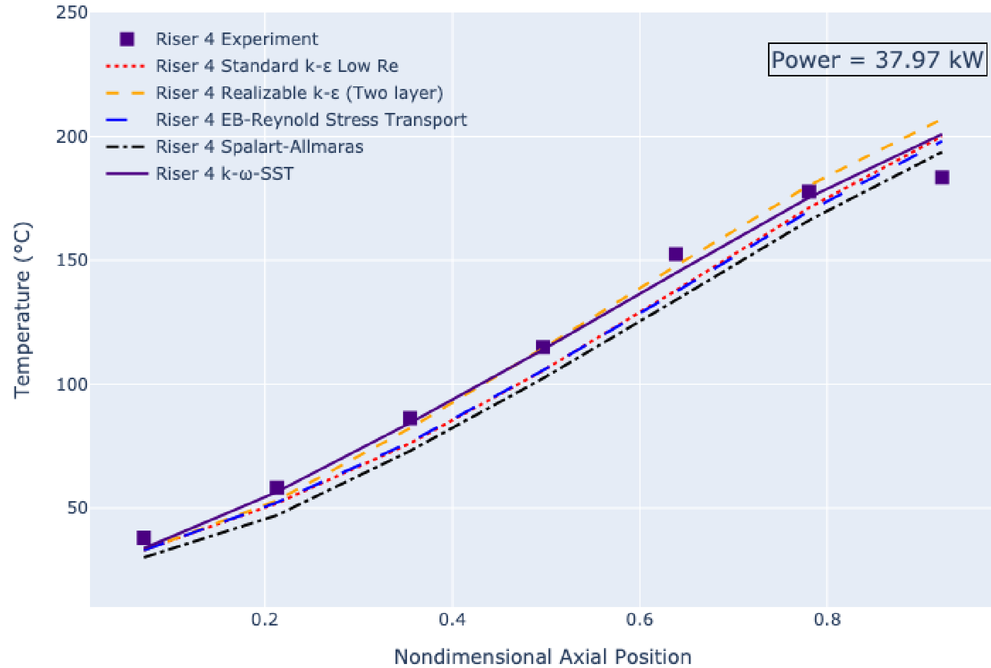

Fig. 23. Effect of the RANS turbulence models on the air centerline temperatures of the 4_{th} riser duct.

perature, $\rho \approx f(T)$, instead of as a function of both pressure and temperature, $\rho = f(p, T)$. As a result, pressure is decoupled from velocity, simplifying the numerical treatment. This decoupling allows the conservation equations to be solved similarly to the incompressible Navier–Stokes equations, with the energy equation solved implicitly and separately from the momentum equations [53].

Figure 24 shows the comparison of the 4_{th} front wall temperature between the Low Mach and Boussinesq approximation compared to experimental measurements. The results show that both Low Mach and Boussinesq approximations are able to predict correct temperature trends. However, the Boussinesq approximation fails to capture the correct values of the temperature distribution.

Figure 25 shows the comparison of the buoyancy modeling strategie for the center of the 4_{th} riser ducts. The Low Mach approximation matches the experimental measurements better

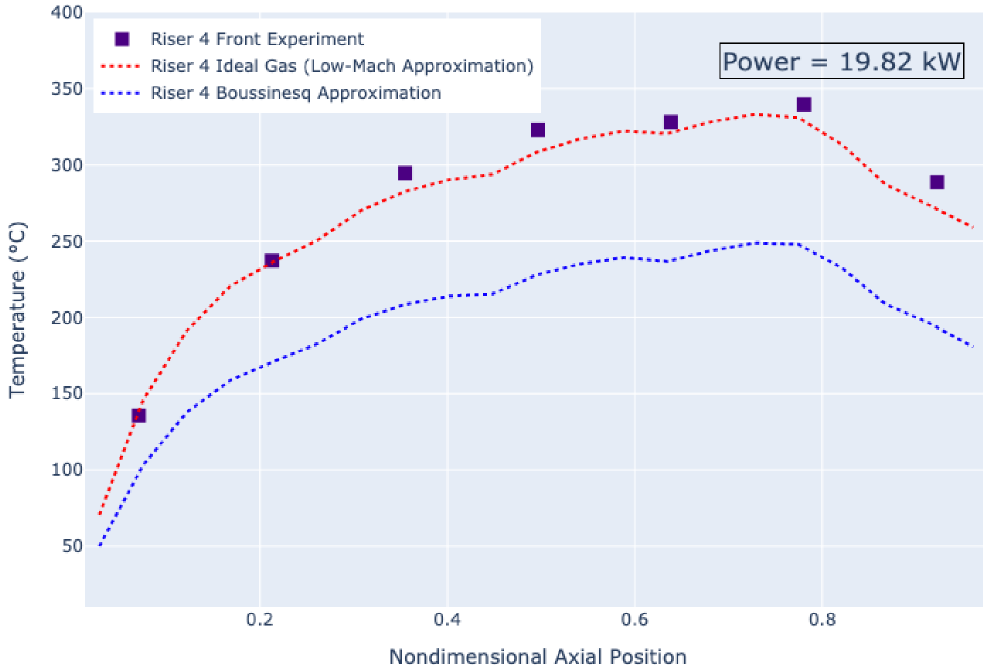

Fig. 24. Natural convection effect of the bouyancy models on the front wall temperatures of the 4_{th} riser duct.

than the results with the Boussinesq approximation. The Boussinesq approximation significantly underestimates the temperature in the channel, which is expected since the wall temperature is also underestimated.

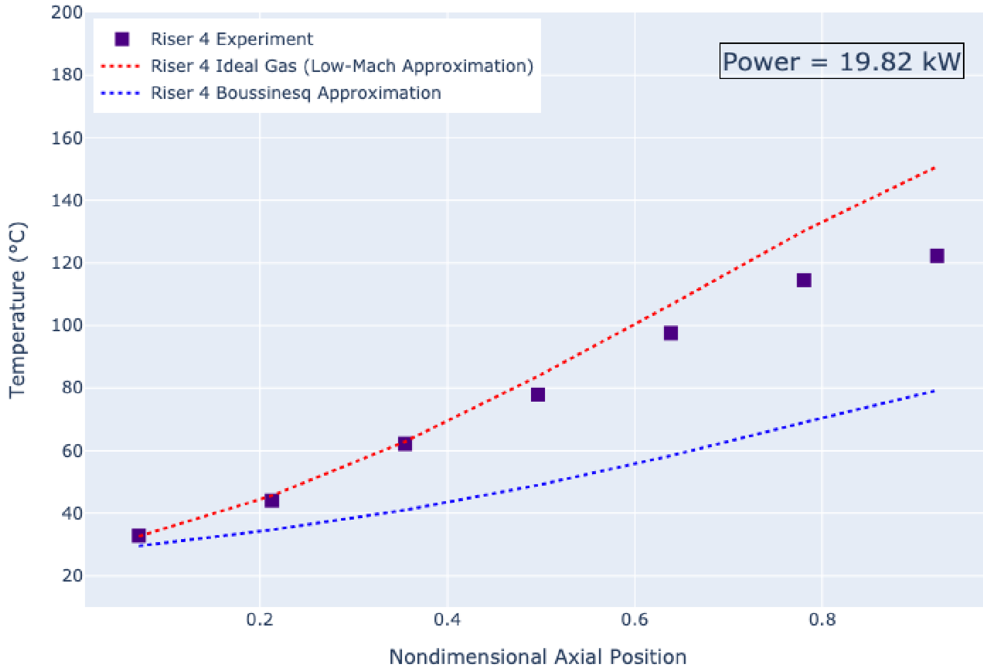

Fig. 25. Natural convection effect of the bouyancy models on the air centerline temperatures of the 4_{th} riser duct.

IV. CONCLUSION

The RCCS is an essential passive safety mechanism that leverages natural convection and radiative heat transfer to lower the RPV temperature during accidents. HTGRs depend on these safety systems for removing decay heat during long transients. Correct design of the RCCS ensures that HTGRs remain inherently safe during loss-of-cooling incidents, as demonstrated by the HTR-PM nuclear power plant. Heat is transferred from the RPV to the riser ducts—mainly through radiation—and is then removed from the riser ducts via natural convection of air. Therefore, understanding the complex interface between radiative heat transfer and natural convection of air is crucial to ensure the effectiveness of these systems.

In this work, the numerical model was validated against the available experimental data from the air-cooled RCCS experimental facility in UW-Madison. The first part of the results focused on validation of natural convection tests for high- and low-power cases under a uniform power profile. For each power level, the comparison began by showing the energy balance, including a mass flow rate comparison between the experiment and the simulation. Next, the wall temperature profiles for the 4th riser were compared. Following this, the front wall temperature differences between the experiment and the simulation, for all risers, were shown in a bar plot. The air centerline temperature profiles for the 4th riser were then compared. The centerline temperature differences for all risers were compared in a bar plot as well. Finally, the wall temperatures of the heated cavity were compared. Based on comparison of the temperatures between experiment and simulation in various locations, the numerical model is able to accurately capture the temperature distribution within the heated cavity and RCCS.

The results show that the $k - \epsilon$ low Reynolds RANS numerical model was able to successfully predict the correct temperature trends and values that were measured in the experiment. The riser duct wall temperatures matched well when comparing the experiment and simulation results. The trends and values observed in the experiments were captured in the numerical model. Most of the deviation occurred at the temperature distribution of the riser duct wall between the first and second axial position, where a sharp temperature gradient was observed.

The sensitivity analysis in the Results section demonstrated the importance of the selected RANS turbulence model in simulating natural convection. To this end, the natural convection case was modeled by using five different RANS turbulence models, and the simulation results were then compared against each other. The wall temperatures and air centerline temperatures in the 4th riser duct were compared. All the models were able to successfully produce the correct trends observed in the experiments. Comparison of the wall temperatures showed that, depending on the turbulence model, wall temperatures can change by up to 50 °C for the RCCS natural convection setup. For the wall temperatures, the standard k-epsilon low Reynolds model matched well with the experimental measurements. Next, the air centerline temperatures were compared for all the models. The selected models underestimated the air centerline temperature, though the k-ω SST model performed better than did the other three models. (It should be noted that the compared values were the time-averaged temperatures in the air centerline and not the bulk values; therefore, the energy balance was consistent between the models.)

The sensitivity analysis to bouyancy modeling showed that boussinesq approximation significantly fails in the modeling of natural convection in the RCCS. The boussinesq approximation significantly underestimates the temperature in the system. Therefore more advanced modeling of the bouyancy such as ideal gas law should be employed in the natural convection modeling of the RCCS.

Based on the simulations conducted in this work, the following recommendations are provided for natural convection modeling the RCCS. These suggestions aim to highlight the key parameters relevant to the modeling of the UW-Madison experimental facility. The simulation parameters are reported in Table III.

- The **standard k-ϵ low-Reynolds-number** model was found to provide accurate turbulence closure for RANS simulations of natural-convection RCCS cases.

- A **wall-resolved approach** was found to be critical for near-wall modeling in natural convection cases, as shown in Figure 7. This approach provides an accurate representation of friction forces, which is essential for estimating the mass flow rate in the system.

- The Boussinesq approximation should not be used for buoyancy modeling in natural convection simulations of the RCCS. It fails to accurately capture temperature profiles in natural convection, as demonstrated in Figures 24 and 25.

- The **heat losses in the upper plenum and exhaust ducts** should be accounted for in the RCCS to achieve accurate results in the RCCS. The heat loss through these parts is approximately 15%, as shown in Table I. It has a substantial impact on natural convection simulations of RCCS, where the mass flow rate is a function of power.

This study contributes to the literature by providing a validated numerical dataset for the UW–Madison experimental RCCS facility. It represents the first complete numerical dataset that includes both the RCCS and the heated cavity within the UW–Madison experimental setup. Additionally, the results highlight significant modeling considerations for natural convection in the RCCS. Modeling choices—such as wall treatment, buoyancy modeling, or turbulence modeling strategies—can lead to substantial temperature differences (around 50 °C), which may result in conservative assumptions during design and safety analyses. These conservative assumptions often increase the cost of system design. CFD-based numerical results can help reduce these conservatisms by achieving a higher-fidelity representation of the system, thereby lowering expenses associated with overly conservative approaches.

Future studies can focus on utilizing the validated model to scenarios with asymmetric heating profiles, where strong flow reversal occurs in the exhaust ducts. The performance of the RANS model under unstable conditions could also be analyzed.

ACKNOWLEDGMENTS

The primary funder of this work was Idaho National Laboratory (INL). The following high-performance computing platform was used in this study.

This research made use of INL computing resources, which are supported by the DOE Office of Nuclear Energy and the Nuclear Science User Facilities under contract no. DE-AC07-05ID14517.

During preparation of this work, the author(s) used ChatGPT and AIVA to improve readability and fix minor grammar issues. After using this tool/service, the author(s) reviewed and edited the content as needed and take(s) full responsibility for the content of the publication.

REFERENCES

[1] D. Lisowski, Q. Lv, B. Alexandreanu, Y. Chen, R. Hu, and T. Sofu, "An Overview of Non-LWR Vessel Cooling Systems for Passive Decay Heat Removal," , Argonne National Laboratory (ANL), IL (United States) (2021); 10.2172/1786964., URL https://www.osti.gov/biblio/1786964.

[2] D.-H. Shin, C. S. Kim, G.-C. Park, and H. K. Cho, "Experimental analysis on mixed convection in reactor cavity cooling system of HTGR for hydrogen production," *International Journal of Hydrogen Energy*, **42**, *34*, 22046 (2017); https://doi.org/10.1016/j.ijhydene.2017.06.232., URL https://www.sciencedirect.com/science/article/pii/S0360319917326757.

[3] Z. Zhang, Y. Dong, F. Li, X. Huang, Y. Zheng, Z. Dong, H. Zhang, Z. Chen, and X. Li, "Loss-of-cooling tests to verify inherent safety feature in the world's first HTR-PM nuclear power plant," *Joule*, **8**, *7*, 2146 (2024); https://doi.org/10.1016/j.joule.2024.06.014., URL https://www.sciencedirect.com/science/article/pii/S2542435124002903.

[4] R. Hu, D. D. Lisowski, M. D. Bucknor, A. R. Kraus, and Q. Lv, "Ambient and building condition effects modeling of air-cooled natural circulation systems," *Applied Thermal Engineering*, **137**, 23 (2018); https://doi.org/10.1016/j.applthermaleng.2018.03.046., URL https://www.sciencedirect.com/science/article/pii/S1359431117371314.

[5] M. Corradini, M. Anderson, M. Muci, Y. Hassan, A. Dominguez, A. Tokuhiro, and K. Hamman, "Thermal-Hydraulic Analysis of an Experimental Reactor Cavity Cooling System with Air. Part I: Experiments; Part II: Separate Effects Tests and Modeling," , Argonne National Laboratory (2014); 10.2172/1183658., URL https://www.osti.gov/biblio/1183658.

[6] D. D. Lisowski, C. D. Gerardi, D. J. Kilsdonk, N. C. Bremer, S. W. Lomperski, R. Hu, A. R. Kraus, M. D. Bucknor, Q. Lv, T. Lee, and M. T. Farmer, "Final Project Report on RCCS Testing with Air-based NSTF," , Argonne National Laboratory (2016); 10.2172/1350591., URL https://www.osti.gov/biblio/1350591.

[7] S. Sulaiman, "Experimental Investigations of Flow Behavior Inside the Upper Plenum of TAMU Air-Cooled Reactor Cavity Cooling System," PhD Thesis (2015).

[8] D. Lisowski, Q. Lv, R. Hu, A. Kraus, N. Bremer, D. J. Kilsdonk, and M. Farmer, "RCCS Testing with the Water-based NSTF: Year-1 Single-Phase Results," , Argonne National Laboratory (ANL), Argonne, IL (United States) (2019); 10.2172/1558600., URL https://www.osti.gov/biblio/1558600.

[9] M. Corradini, M. Anderson, Y. Hassan, and A. Tokuhiro, "Experimental Studies of NGNP Reactor Cavity Cooling System With Water," , Univ. of Wisconsin, Madison, WI (United States); Texas A & M Univ., College Station, TX (United States); Univ. of Idaho, Moscow, ID (United States); Idaho National Laboratory (INL), Idaho Falls, ID (United States) (2012); 10.2172/1063993., URL https://www.osti.gov/biblio/1063993.

[10] S. Lomperski, W. Pointer, C. Tzanos, T. Y. Wei, and A. Kraus, "Generation IV nuclear energy system initiative; air-cooled option RCCS studies and NSTF preparation." , Argonne National Lab.(ANL), Argonne, IL (United States) (2012).

[11] D. D. Lisowski, A. R. Kraus, M. D. Bucknor, R. Hu, and M. T. Farmer, "Experimental observations of natural circulation flow in the NSTF," *Nuclear Engineering and Design*, **306**, 124 (2016); https://doi.org/10.1016/j.nucengdes.2016.01.014., URL https://www.sciencedirect.com/science/article/pii/S0029549316000248, 7th International Topical Meeting on High Temperature Reactor Technology (HTR 2014).

[12] D. D. Lisowski, C. D. Gerardi, R. Hu, D. J. Kilsdonk, N. C. Bremer, S. W. Lomperski, A. R. Kraus, M. D. Bucknor, and M. T. Farmer, "Water NSTF Design, Instrumentation, and Test Planning," , Argonne National Laboratory (2017); 10.2172/1375452., URL https://www.osti.gov/biblio/1375452.

[13] D. D. Lisowski, T. Lee, D. J. Kilsdonk, N. C. Bremer, C. D. Gerardi, S. W. Lomperski, and M. T. Farmer, "Status Report on the Water-Based NSTF RCCS Capability: Preparations and Design for the Transformation of the Natural Convection Shutdown Heat Removal Test Facility (NSTF) From Air to Water-based Cooling," , Argonne National Laboratory (ANL), Argonne, IL (United States) (2015); 10.2172/1512941., URL https://www.osti.gov/biblio/1512941.

[14] C. P. Tzanos and M. T. Farmer, "Feasibility study for use of the natural convection shutdown heat removal test facility (NSTF) for VHTR water-cooled RCCS shutdown." , Argonne National Laboratory (ANL) (2007); 10.2172/932941., URL https://www.osti.gov/biblio/932941.

[15] D. Lisowski, Q. Lv, N. Bremer, R. Hu, A. Kraus, D. Kilsdonk, S. Lomperski, and M. Farmer, "Report on Year-2 of Water NSTF Matrix Testing," , Argonne National Laboratory (ANL), Argonne, IL (United States) (2020); 10.2172/1782658., URL https://www.osti.gov/biblio/1782658.

[16] Q. Lv, D. Lisowski, M. Jasica, R. Hu, A. Kraus, Z. J. Ooi, N. Bremer, and M. Farmer, "Report on Year-3 of Water NSTF Matrix Testing: Two-Phase Parametric Test Series," , Argonne National Laboratory (ANL), Argonne, IL (United States) (2021); 10.2172/1828379., URL https://www.osti.gov/biblio/1828379.

[17] Q. Lv, M. Jasica, R. Hu, Z. Ooi, M. Farmer, and D. Lisowski, "Report on Year-4 of Water NSTF Matrix Testing: Facility Maintenance and Accident Testing," , Argonne National Laboratory (ANL), Argonne, IL (United States) (2022); 10.2172/1897962., URL https://www.osti.gov/biblio/1897962.

[18] A. Manera, M. Corradini, V. Petrov, M. Anderson, C. Tompkins, and D. Nunez, "Model validation using CFD-grade experimental database for NGNP Reactor Cavity Cooling Systems with water and air," , Univ. of Michigan, Ann Arbor, MI (United States) (2018); 10.2172/1420273., URL https://www.osti.gov/biblio/1420273.

[19] S. A. Sulaiman, E. E. Dominguez-Ontiveros, T. Alhashimi, J. L. Budd, M. D. Matos, and Y. A. Hassan, "Design considerations and experimental observations for the TAMU air-cooled reactor cavity cooling system for the VHTR," *AIP Conference Proceedings*, **1659**, *1*, 030002 (2015); 10.1063/1.4916850., URL https://doi.org/10.1063/1.4916850.

[20] R. Vaghetto and Y. A. Hassan, "Experimental Investigation of a Scaled Water-Cooled Reactor Cavity Cooling System," *Nuclear Technology*, **187**, *3*, 282 (2014); 10.13182/NT13-130., URL https://doi.org/10.13182/NT13-130.

[21] R. Vaghetto, "Experimental and Computational Study of a Scaled Reactor Cavity Cooling System," PhD Thesis, Texas A&M University (2013).

[22] L. Capone, Y. A. Hassan, and R. Vaghetto, "Reactor cavity cooling system (Rccs) experimental characterization," *Nuclear Engineering and Design*, **241**, *12*, 4775 (2011); https://doi.org/10.1016/j.nucengdes.2011.07.043., URL https://www.sciencedirect.com/science/article/pii/S0029549311006194, the18th International Conference on Nuclear Engineering (ICONE-18).

[23] M. S. Sena and Y. A. Hassan, "Thermal-hydraulic behavior simulations of the reactor cavity cooling system (RCCS) experimental facility using Flownex," *Nuclear Engineering and Technology*, **55**, *9*, 3320 (2023); 10.1016/j.net.2023.05.023., URL https://www.sciencedirect.com/science/article/pii/S1738573323002498.

[24] Y.-Y. Bae, S.-D. Hong, and Y.-W. Kim, "Scaling analysis of PMR200 reactor cavity cooling system," *Nuclear Engineering and Design*, **271**, 523 (2014); https://doi.org/10.1016/j.nucengdes.2013.12.027., URL https://www.sciencedirect.com/science/article/pii/S0029549313007073, sI : HTR 2012.

[25] J.-H. Kima, Y.-Y. Bae, C.-S. Kima, S.-D. Honga, and E.-S. Kima, "The Results of the Third NACEF Test for the RCCS Verification," .

[26] C. S. Kim, D. Lisowski, Y. Y. Bae, J. H. Kim, and S. N. Lee, "Comparative study with two reduced test facilities for air-cooled RCCS scaling law," *Nuclear Engineering and Design*, **380**, 111276 (2021); https://doi.org/10.1016/j.nucengdes.2021.111276., URL https://www.sciencedirect.com/science/article/pii/S0029549321002284.

[27] R. Hu, A. Kraus, M. Bucknor, Q. Lv, and D. Lisowski, "Final Project Report on Computational Modeling and Analysis of Air-Based NSTF," , Argonne National Laboratory (2016); 10.2172/1429403., URL https://www.osti.gov/biblio/1429403.

[28] P. Rousseau, C. du Toit, J. Jun, and J. Noh, "Code-to-code comparison for analysing the steady-state heat transfer and natural circulation in an air-cooled RCCS using GAMMA+ and Flownex," *Nuclear Engineering and Design*, **291**, 71 (2015);

https://doi.org/10.1016/j.nucengdes.2015.05.004., URL https://www.sciencedirect.com/science/article/pii/S0029549315001910.

[29] Y. A. H. Angelo Frisani and V. M. Ugaz, "Computational Fluid Dynamics Analysis of Very High Temperature Gas-Cooled Reactor Cavity Cooling System," *Nuclear Technology*, **176**, *2*, 238 (2011); 10.13182/NT11-A13299., URL https://doi.org/10.13182/NT11-A13299.

[30] O. Koekemoer, C. du Toit, and P. Niemand, "Investigation into different 1D/3D co-simulation methodologies applied to a natural circulation loop," *Nuclear Engineering and Design*, **390**, 111698 (2022); https://doi.org/10.1016/j.nucengdes.2022.111698., URL https://www.sciencedirect.com/science/article/pii/S0029549322000528.

[31] R. Freile, M. Tano, P. Balestra, S. Schunert, and M. Kimber, "Improved natural convection heat transfer correlations for reactor cavity cooling systems of high-temperature gas-cooled reactors: From computational fluid dynamics to Pronghorn," *Annals of Nuclear Energy*, **163**, 108547 (2021); https://doi.org/10.1016/j.anucene.2021.108547., URL https://www.sciencedirect.com/science/article/pii/S0306454921004230.

[32] D.-H. Shin, S.-Y. Kim, C. S. Kim, G.-C. Park, and H. K. Cho, "Study on the Turbulent Mixed Convection Phenomena Inside the Air-Cooled RCCS Riser," , vol. Volume 6B: Thermal-Hydraulics and Safety Analyses of *International Conference on Nuclear Engineering*, V06BT08A029 (2018); 10.1115/ICONE26-82071., URL https://doi.org/10.1115/ICONE26-82071.

[33] S.-Y. Kim, C.-S. Kim, and H. K. Cho, "Local flow structure and turbulence quantities inside a heated rectangular riser in turbulent forced and mixed convection heat transfers," *Experimental Thermal and Fluid Science*, **122**, 110297 (2021); https://doi.org/10.1016/j.expthermflusci.2020.110297., URL https://www.sciencedirect.com/science/article/pii/S0894177720307986.

[34] Q. Lv, A. Kraus, Z. J. Ooi, R. Hu, and D. Lisowski, "Progress on Computational Modeling of Water-Based NSTF (FY2021)," , Argonne National Laboratory (ANL), Argonne, IL (United States) (2021); 10.2172/1825925., URL https://www.osti.gov/biblio/1825925.

[35] Z. J. Ooi, Q. Lv, R. Hu, M. Jasica, and D. Lisowski, "FY22 Progress on Computational Modeling of the Water-Based NSTF," , Argonne National Laboratory (ANL), Argonne, IL (United States) (2022); 10.2172/1888758., URL https://www.osti.gov/biblio/1888758.

[36] Z. J. Ooi, Q. Lv, M. J. Jasica, R. Hu, and D. D. Lisowski, "FY23 Progress on Computational Modeling of the Water-Based NSTF," , Argonne National Laboratory (ANL), Argonne, IL (United States) (2023); 10.2172/2007810., URL https://www.osti.gov/biblio/2007810.

[37] Z. J. Ooi, Q. Lv, R. Hu, M. Jasica, and D. Lisowski, "Effect of inlet throttling on thermohydraulic instability in a large scale water-based RCCS: A system-level analysis with RELAP5-3D," *Nuclear Engineering and Technology*, **56**, *5*, 1902 (2024); https://doi.org/10.1016/j.net.2023.12.053., URL https://www.sciencedirect.com/science/article/pii/S1738573323006058.

[38] S. B. Pope, *Turbulent Flows*, Cambridge University Press (2000); 10.1017/CBO9780511840531.

[39] P. SPALART and S. ALLMARAS, *A one-equation turbulence model for aerodynamic flows*; 10.2514/6.1992-439., URL https://arc.aiaa.org/doi/abs/10.2514/6.1992-439.

[40] S. D. I. Software, "Simcenter STAR-CCM+ User Guide, version 2021.1," *Adaptive Mesh Refinement for Overset Meshes*, 3067–3070, SiemensURL https://docs.sw.siemens.com/documentation/external/PL20200805113346338/en-US/userManual/userguide/html/STARCCMP/GUID-28A739CF-6DE2-4D87-B582-E390B522011C.html#.

[41] "The prediction of laminarization with a two-equation model of turbulence," *International Journal of Heat and Mass Transfer*, **15**, *2*, 301 (1972); https://doi.org/10.1016/0017-9310(72)90076-2.

[42] W. Rodi, "Experience with Two-Layer Models Combining the k-e Model with a One-Equation Model Near the Wall," *29th Aerospace Sciences Meeting*, AIAA 91-0216, Reno, NV, AIAA (1991).

[43] T.-H. Shih, W. Liou, A. Shabbir, Z. Yang, and J. Zhu, "A New k-ϵ Eddy Viscosity Model for High Reynolds Number Turbulent Flows – Model Development and Validation," TM 106721, NASA (1994).

[44] D. C. Wilcox, *Turbulence Modeling for CFD*, DCW Industries, La Canada, CA (1995).

[45] D. Wilcox, *Turbulence Modeling for CFD*, DCW Industries, Inc (1998).

[46] F. Menter, "Two-equation eddy-viscosity turbulence modeling for engineering applications," *AIAA Journal*, **32**, *8*, 1598 (1994).

[47] P. R. Spalart and C. L. Rumsey, "Effective Inflow Conditions for Turbulence Models in Aerodynamic Calculations," *AIAA Journal*, **45**, *10*, 2544 (2007); 10.2514/1.29373.

[48] S. Sarkar and L. Balakrishnan, "Application of a Reynolds-Stress Turbulence Model to the Compressible Shear Layer," NASA Contractor Report ICASE Report 90-18, NASA CR 182002, Institute for Computer Applications in Science and Engineering (ICASE), NASA Langley Research Center, Hampton, VA, USA (1990)URL https://ntrs.nasa.gov/archive/nasa/casi.ntrs.nasa.gov/19900010221.pdf.

[49] R. Manceau and K. Hanjalić, "Elliptic blending model: A new near-wall Reynolds-stress turbulence closure," *Physics of Fluids*, **14**, *2*, 744 (2002); 10.1063/1.1432693.

[50] S. Lardeau and R. Manceau, "Computations of Complex Flow Configurations Using a Modified Elliptic-Blending Reynolds-Stress Model," *Proceedings of the 10th Engineering Turbulence Modelling and Measurements Conference (ETMM10)*, Marbella, Spain (2014)URL https://hal.science/hal-01051799/file/1712.pdf.

[51] "CUBIT," https://cubit.sandia.gov (2022).

[52] S. Okyay, D. Reger, V. Coppo Leite, E. Merzari, P. Balestra, and G. Strydom, "High-Fidelity Forced Convection Simulations of the University of Wisconsin-Madison Air-Cooled Reactor Cavity Cooling System," *Nuclear Engineering and Design* (2025)Accepted for publication.

[53] T. Nguyen, *High Fidelity Simulation of Buoyancy-Driven Fluid Flow in Flouride Salt-Cooled High Temperature Reactors Using the Spectral Element Method*, The Pennsylvania State University (2023).